Chinese Chemical Letters 33 (2022) 2783–2798

Contents lists available at ScienceDirect

Chinese Chemical Letters

journal homepage: www.elsevier.com/locate/cclet

Light-guided tumor diagnosis and therapeutics: From nanoclusters to polyoxometalates

Xiaofeng Fan[a,1], Wei Pang[a,1], Hao Feng[e,1], Ruiyi Zhang[a], Wentao Zhu[a], Qiushi Wang[b,c], Jun Miao[a,b,*], Yiwen Li[c,*], Yanjun Liu[d,*], Xiaoqian Xu[a,*]

[a] Key Laboratory of Cell Biology, Ministry of Public Health and Key Laboratory of Medical Cell Biology, Ministry of Education, China Medical University, Shenyang 110122, China
[b] Guangdong Provincial Key Laboratory of Catalysis, Shenzhen Grubbs Institute and Department of Chemistry, Southern University of Science and Technology, Shenzhen 518000, China
[c] School of Materials Science and Engineering, Hubei University, Wuhan 430062, China
[d] Department of Electrical and Electronic Engineering, Southern University of Science and Technology, Shenzhen 518000, China
[e] Department of Ophthalmology, The First Affiliated Hospital of China Medical University, Shenyang 110001, China

ARTICLE INFO

Article history:
Received 14 November 2021
Revised 4 December 2021
Accepted 22 December 2021
Available online 27 December 2021

Keywords:
Polyoxometalates
Light-guided nanoagents
Nanoclusters
Metal oxides clusters
Photothermal therapy
Photodynamic therapy

ABSTRACT

Malignant tumors, with the characteristics of easy metastasis and recurrence, are a serious threat to health of mankind. It is urgent to develop promising clinical cancer targeted agents with combination of rapid diagnosis and efficient therapies. Compared with the conventional photosensitizing agents, the recent advances of nanoagents based on transition metal-oxide clusters possess unique structural and electronic properties, greatly improving cancer survival rate, meanwhile, keeping high contrast imaging. This review provides a brief introduction of metal-oxide clusters, including both nanoclusters to molecular clusters, specifically polyoxometalates (POMs). Subsequently, biocompatibility of metal-oxide clusters is emphasized from aspects of endocytosis, macropinocytosis, and phagocytosis. Through the classification of late and early transition metals oxide clusters, recent outcomes of light-guided nanoagents are represented with their intriguing chemical and optical properties in their diagnosing and photochemotherapy performance. It shed light on the summary of next generation multifunctional cancer targeting agents' developments as well as outlook of materials selection trends and research direction in the future.

1. Introduction

With the development of nanotechnology, phototherapy mediated by nanomaterials, as a new tumor diagnosis and therapeutic mode, has shown great potential for transforming medicine and clinical applications [1–10]. Since the laser source used in phototherapy is often with low energy and can achieve controllable irradiation of targeted tumor areas, one of the most remarkable features of phototherapy is minimally invasive, thus the patient will not feel pain during the therapeutic process [11–13]. The heat produced during the therapeutic process only has the effect on the surrounding cells, which is controllable, decreasing systemic damage, in comparison with the systemic toxicity of traditional chemotherapy or radiotherapy, and will not cause drug resistance [14,15]. In addition, some nanoagents with photothermal conversion abilities can also be navigated and assisted in diagnosis and treatment by multi-model imaging methods [16–22]. Therefore, the diagnosis and therapeutic methods based on newly developed nanotechnology is expected to become promising and effective diagnoses and therapeutic models in tumors (Fig. 1) [23–25].

Photothermal therapy (PTT) and photodynamic therapy (PDT) are the most commonly employed phototherapy approaches. PTT is a kind of high-temperature treatment for cancer, based on light-absorbing agents [16,26-28]. It is generally simulated by near-infrared light (NIR), during which the light energy can be converted into heat energy by the agents [14,29,30]. The local heat generated can kill cancer cells without affecting normal tissues. Due to the weak invasive property, PTT attracts increasing attention in biomedical applications [17,31]. Moreover, chemotherapy combined with PTT can improve the curative effect by reducing the usage of drugs [18]. Due to the synergistic effect of photochemotherapy, the dosage of chemotherapeutic agents

* Corresponding authors.
E-mail addresses: 11653002@mail.sustech.edu.cn (J. Miao), yiwenli@hubu.edu.cn (Y. Li), yjliu@sustech.edu.cn (Y. Liu), xqxu@cmu.edu.cn (X. Xu).
[1] These authors contributed equally to this work.

https://doi.org/10.1016/j.cclet.2021.12.057
1001-8417/

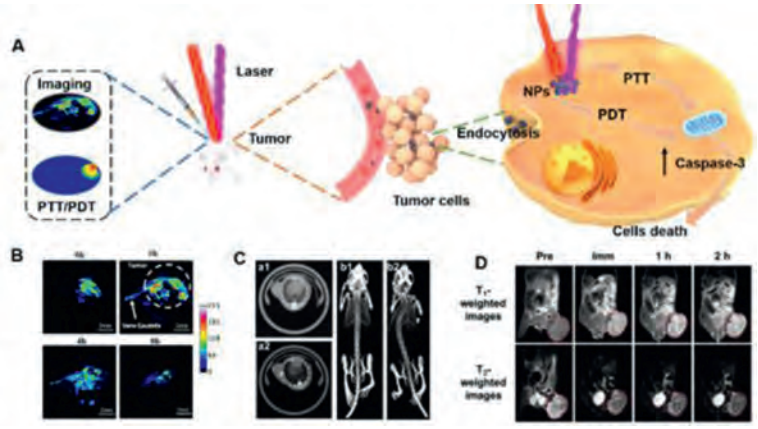

Fig. 1. (A) Schematic representation of PAI-guided PTT and PDT synergistic treatment. (B) Real-time PAI of mice after systemic administration of L-Cys-MoO_{3-x} NPs (100 μL, 200 μg/mL) through intra-tumor injection. (C) *In vivo* X-ray transverse CT images of tumor (a1, a2) and 3D renderings of *in vivo* CT images (b1, b2) before (a1, b1) and after (a2, b2) intratumoral injection of PEGylated$WO_{2.9}$ NRs. (D) *In vivo* T_1- and T_2-weighted MR images of MKN-45 tumor-bearing mice obtained before (Pre) and after (immediate, 1 h, and 2 h) the intravenous injection of Mn_3O_4-coated Fe_3O_4 hybrid nanocrystal. (A, B) Reproduced with permission [23]. Copyright 2021, Elsevier. (C) Reproduced with permission [24]. Copyright 2014, Scientific Reports. (D) Reproduced with permission [25]. Copyright 2016, Elsevier.

can be substantially reduced, and the adverse effects caused by chemotherapeutic agents can be also lessened [32,33].

In addition to PTT, PDT is one of the most successful treatment for a varied spectrum of cancers [20,34-36]. PDT requires the synergy of three elements: photosensitive agents uptaken by receptor cells; proper exciting light, and existence of oxygen. The light-activated photosensitive agents transfer its excited-state energy to the surrounding oxygen for generating reactive oxygen species (ROS), which cause cancerous cells to perish directly or indirectly, *via* the induction of tumor vascular stasis [21,37].

Along with efficient phototherapy, the *in situ* rapid diagnosis can also be achieved, as many therapeutic agents can be also used as the contrast agents due to their excellent light absorption capability. The photoacoustic effect provides the possibility to achieve a high contrast imaging method as well as deep penetrability in tissue due to ultrasound signal conversion [38–40]. It improves the signal to noise ratio compared to optical imaging due to avoiding the light scattering and dissipation in tissue [16,41], which is widely employed in monitoring tumor growth. Due to the high optical absorption of hemoglobin molecules, photoacoustic imaging (PAI) can also reveal the distribution and dynamics of blood in tissues and classify malignant lesions according to tumor-associated angiogenesis and hypoxia [22,42,43], which can be used to monitoring tumor metastasis. Other imaging methods, computed tomography (CT) imaging and magnetic resonance imaging (MRI), can also be mediated by contrast agents and employed to monitoring the tumor changes during the treatment [44–46].

There are many candidates in photochemotherapy research areas, which serve as both ablation agents and contrast agents [47,48]. In comparison with organic agents, inorganic clusters meet the requirements for excellent photo-guided nanoagents with better photostability, increased immunogenicity, higher biocompatibility, and lower toxicity. However, the commonly used ablation agents and contrast agents also suffered from various drawbacks. For instance, the carbon-based nanoagents are lack in strong molar extinction cross-section in NIR window peak position [48–50], metallic nanoagents possess high light absorption based localized surface plasmon resonances (LSPR) but require laborious process and high-cost fabrication [51], semiconductor quantum dots such as CdSe with higher quantum yield would decrease the thermal conversion in imaging and therapy, and show a high toxicity to testis tissues [52,53]. Therefore, the excellent inorganics, balancing strong optical absorbance with photothermal and thermoacoustic conversion efficiency, as well as bioactive properties, are urgent to be developed and improved.

Transition metal oxide clusters, including early transition metal oxide clusters, mostly polyoxometalates (POMs), and other late transition metal oxide nanoclusters have shown great advantages in the integrated research on tumor diagnosis and treatment because the nature of metal-oxygen bonding in transition metal oxide clusters, which results in their unique structural and electronic properties. The physicochemical properties of transition metal oxide clusters are strongly related to their outer *d* electrons leading to multiple bands. Their broaden optical transitions in the full spectrum could be attributed to plasmon, polaron, charge transfer and d-d transition, which provides versatile strategies for photochemotherapy [54–56]. The tunable and large absorption cross-section in NIR I and II biological window, non-radiation recombination for carrier relaxation, ease of fabrication methods could promote transition metal oxide clusters as distinguished photosensitizing agents in their potential biomedical applications [57–59]. Moreover, the multifunctional clusters-based nanocomposites, integrating transition metal oxide clusters with other bioactive chemicals, make possibility to achieve efficient diagnosis and synergetic therapy. Differed from late transition metal oxide nanoclusters [60], POMs are a family of early transition metal oxide molecular clusters, which are composed of MO_x (M = usually Mo and W; less commonly V, Nb and Ta; x = 5, 6) as basic construction units, except a few examples of aluminum and titanium oxide clusters [61,62]. POMs can assemble from small single clusters (1 nm) to big aggregates (tens of nanometer) [63] in both mild acidic and reductive solution, as exemplified by the heteropoly blue solutions known for centuries. Tailored to the tumor microenvironment (TME) featuring both mild acidity and reducibility, POMs favor their intratumoral accumulation and enhanced photothermal conversion in response to the intratumoral acidity and reducibility, showing an excellent tumor-specific photo-hyperthermia. Meanwhile, POMs also possess the properties, such as cell wall/membrane disruption, inhibition of intracellular respiratory chain dehydrogenases (RCD) activity, destruction of ROS and depletion of glutathione (GSH) [64], which have enormous potential of integrative collaborative treatment. Distinct from the well-investigated nanocluster-based agents, unique electronic structures of POMs are considered as the origin of the observed acidity-induced self-assembly and reduction-promoted NIR absorbance.

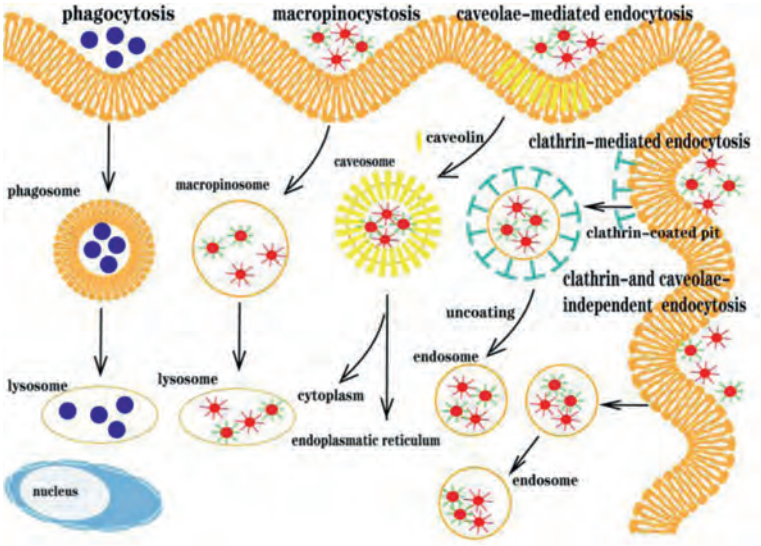

Fig. 2. Schematic diagram of cellular uptake and cytokinesis pathways of nanoparticles. Nanoparticles enter cells through five types of pathways: (1) Nanoparticles <100–150 nm enter through clathrin- and caveolae-independent endocytosis; (2) Nanoparticles < 100–150 nm enter mainly through clathrin-mediated endocytosis; (3) Nanoparticles < 200–500 nm mainly by caveolae-mediated endocytosis; (4) Nanoparticles 0.5–5 μm mainly by macropinocytosis; (5) Large particles mainly by macrophage, neutrophil and monocyte-mediated phagocytosis.

To bridge the traditional concepts of molecular clusters (POMs) and nanoclusters in light-guided tumor diagnosis and therapeutics, biocompatibility of POMs and nanoclusters and their functions in cancer diagnoses and therapeutics are summarized respectively in this review. Overall, the physiochemical factors for the diagnosis and therapy improvement could be available by the development of low toxic efficient cancer photosensitizing agents in the region of transition metal oxide clusters.

2. Biocompatibility of transition metal-oxide clusters

Biocompatibility analysis is a crucial aspect to assure that the toxic effects of the metal oxide cluster-based agents do not suppress their advantages in prospects for the future application. Therefore, the biocompatibility of the nanoagents were extensively investigated, including: (1) cell-dependent toxicity and cellular ultrastructure damages *in vitro*; (2) main organ damages, as well as biodistribution and clearances.

2.1. Cyto-toxicity

For transition metal oxide clusters, the cyto-toxicity is usually dose-dependent, as the concentrations mainly influence the quality of the culture medium. The cyto-toxicity is also highly associated with particle size and surface modification, which can also determine how the nanoparticles enter the cells. Generally, positively charged, and neutral nanoparticles are more accessible to the cells, as the membrane are negatively charged. Determined by the particle size, clathrin-mediated endocytosis, caveolae-dependent endocytosis, pinocytosis, and phagocytosis are the main cellular uptake pathways of nanoparticles (Fig. 2).

After nanoagents internalize into the cell, cell survival rate above 85% is generally considered as a safe concertation for biological experiments, while Cell Counting Kit-8 (CCK), 3-(4,5-dimethylthiazol-2-yl)−2,5-diphenyltetrazolium bromide (MTT), bio-transmission electron microscope (Bio-TEM) and CellTiter-Glo (CTG) are the widely used methods to assess the cyto-toxicity. For example, Shen and coworkers have studied the toxicity of titanium dioxide/poly(ethylene glycol) double acrylates (TiO_2/PEGDA) NPs on human cervical cancer cells (HeLa) (Fig. 3A). Cell survival rates were 82.2%, 67.5% and 56% at 0.03, 0.3 and 3 mol/L respectively, which exhibited the dose-dependent results, and indicate that lower than 0.03 mol/L of TiO_2/PEGDA can be applied into biological applications [65].

For tungsten oxide nanoclusters, Yi *et al.* have compared the cytotoxicity of $W_{18}O_{49}$@lentinan nanorods ($W_{18}O_{49}$@LTN NRs) and $W_{18}O_{49}$ NRs on human breast cancer cells (MDA-MB-231). Results in Fig. 3B showed that 200 μg/mL of $W_{18}O_{49}$@LTN NRs is the LC10 (10% lethal concentration) while 100 μg/mL of $W_{18}O_{49}$ NRs is the LC10 for the same tumor cell line. Obviously, modification by LNT on $W_{18}O_{49}$ NRs helps to decrease the cytotoxicity [66]. Cytotoxicity of manganese oxide nanoclusters, such as MnO_2@Ce6@PDA-FA, chlorine e6 (Ce6) loaded MnO_2-polyethylene glycol (PEG) (Ce6@MnO_2-PEG), BSA-MnO_2 NPs (BSA = Bovine serum albumin), *etc.*, were also reduced with surface modification. In 2016, Liu *et al.* studied the toxicity of Ce6@MnO_2-PEG at concentration range of 1.5–100 × 10^{-6} mol/L on mouse breast cancer cells (4T1) and 100 μmol/L was determined as the LC10 for further biological applications (Fig. 3C) [67]. In 2018, Song *et al.* evaluated the toxicity of BSA-MnO_2 NPs on human umbilical vein endothelial cells (HUVEC) and human mammary epithelial cells (MCF-10A). Up to 300 mg/mL BSA-MnO_2 NPs, no significant cell death were obtained, which indicated that modification with BSA avails the biocompatibility of the materials [68]. In 2020, MnO_2-based nanocomposite nanoparticles, MnO_2@Ce6@PDA-FA (MCPF NPs), fabricated by Mei was investigated in their cytotoxicity on human breast cancer cells (MCF-7), HeLa and human nasopharyngeal epithelial cells (NP69). Cell viability remained higher than 85% at a concentration of 200 μg/mL for all the cell types, which indicates that the cytotoxicity of MCPF NPs is significantly reduced and suitable for biological experiments under a concentration of 200 μg/mL [69]. A similar example of BSA decoration also goes to BSA-coated $Na_9[GdW_{10}O_{36}]$ [70]. The abovementioned examples also indicate that BSA is a preferable candidate for modification of early transition metal oxide nanoclusters to reduce their cytotoxicity. In 2021, Mahboubeh Rostami *et al.* developed a micelle carrier using biotin-targeted stearic acid-polyethylene glycol (SPB) polymer coupling as an Anderson-type manganese polyoxomolybdate (TRIS-MnPOMo) [71], which was evaluated by MTT assay against MCF-7, MDA-MB-231 and HUVEC for cytotoxicity. Dose-dependent cytotoxicity

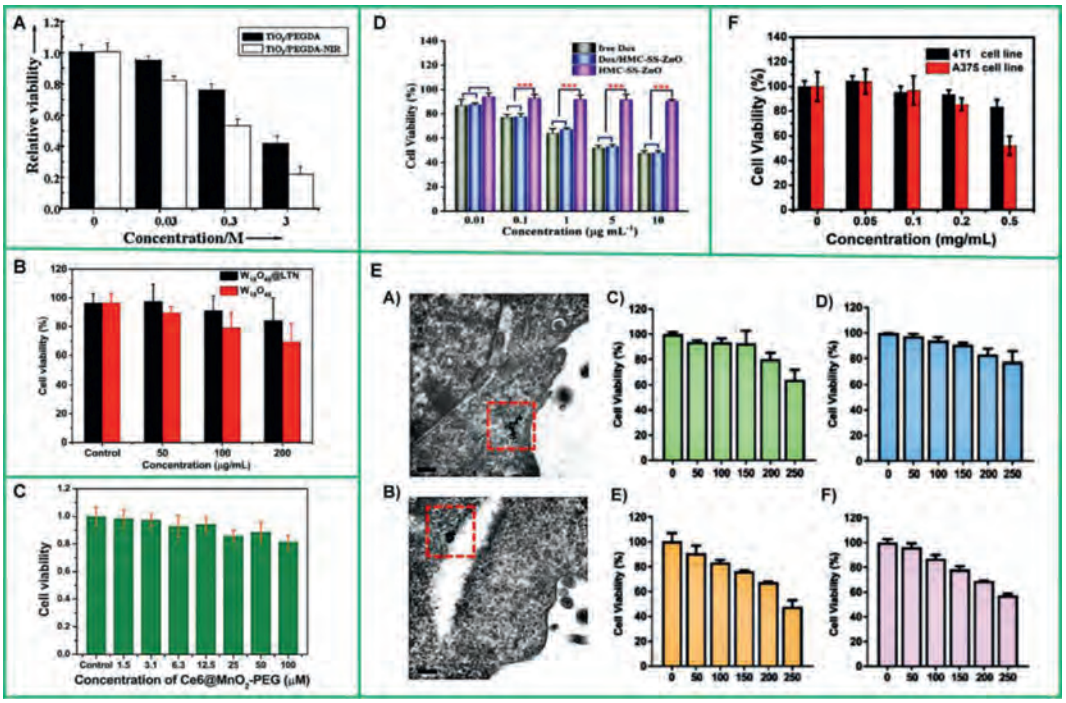

Fig. 3. Toxicity evaluation of different concentrations of transition metal oxides on tumor cells. (A) Viability of TiO_2/PEGDA on HeLa cells. Reproduced with permission [65]. Copyright 2013, American Chemical Society. (B) Viability of $W_{18}O_{49}$@LTNNRs and $W_{18}O_{49}$NRs on MDA-MB-231 cells. Reproduced with permission [66]. Copyright 2019, Elsevier. (C) Viability of Ce6@MnO_2-PEG on 4T1 cells. Reproduced with permission [67]. Copyright 2014, Royal Society of Chemistry. (D) Viability of Dox/HMC-SS-ZnO on 4T1 cells. Reproduced with permission[72]. Copyright 2018, American Chemical Society. (E) Viability of chiral MoO_{3-x} NPs on HeLa cells. Reproduced with permission [74]. Copyright 2019, Wiley-VCH Verlag GmbH & Co. KGaA. (F) Viability of pCo_3O_4 NPs on 4T1 and A375 cells. Reproduced with permission [81]. Copyright 2020, Elsevier.

was also observed in all groups of both cell lines (free drug and nanoformulations). The best cytotoxicity results could be found for TRISM-MnPOMo coupled by SPB at a concentration of 200 μg/mL.

Surface coating with mesoporous material can reduce intrinsic toxicity profile of transition metal oxide clusters. For example, an example of zinc oxide clusters was reported to be genotoxic, and preparation of their nanocomposites (*e.g.*, HMC-SS-ZnO [72], UZNPs-PAA-DOX agents (DOX = doxorubicin) [73]) can lead to reduction in cytotoxicity and provide them with biological application prospects. In 2019, Wang and co-authors reported the toxicity of HMC-SS-ZnO on 4T1 cells and further determined that 10 μg/mL was the LC10 for safe biological applications (Fig. 3D).

Cytotoxicity of the same transition metal oxide nanoclusters but with different in particle size and reducibility were also varied. In 2019, our group and collaborators have fabricated MoO_{3-x} NPs with different chirality. CCK8 assay were employed to assess the toxicity of chiral MoO_{3-x} NPs on HeLa cells. As shown in Figs. 3E-C and 3E-D, LC10 for L/D-Cys-$MoO_{2.8}$ NPs which adopt a particle size about 2.8 nm are below 200 μg/mL. As comparison in Figs. 3E-E and 3E-F, 50 μg/mL is the LC10 of L-/D-Cys-MoO_2 [74]. Authors also studied the cytotoxicity of D-/L-Cys-$MoO_{2.8}$ on HeLa cells at different time points (4 h, 24 h and 48 h), and not significantly change in cell viability was obtained around 200 μg/mL. This indicates that its accuracy and low chronic cytotoxicity are stable and suitable for biomedical applications *in vivo* [23].

Group VIIIB transition metal oxides, including nickel, cobalt, and iron oxide nanoclusters, are belonging to the magnetic nanoagents. Due to the abundance of valence states and forms of iron, it can be packaged and complexed with a variety of substances (*e.g.*, Fe_3O_4 NPs, Fe_3O_4@PDA@BSA-Bi_2S_3, Fe_3O_4@Ag [75], porous iron oxide nanoagents (PIONs) [76], folic acid-Au nanocages (F-AUNC@Fe_3O_4) [77], Fe_3O_4@Au [78], *etc.*) (see Table 1 for toxicity), widely used in anti-tumor research, and can be combined with photochemotherapy and magnetocaloric therapy. In 2014, Yang *et al.* investigated the toxicity of individual and clustered magnetic Fe_3O_4 NPs on human lung adenocarcinoma epithelial cell line (A549), and at 500 μg/mL of both individual and clustered magnetic Fe_3O_4 NPs, cell viability was maintained at approximately 92.63%, neither of which exhibited high cytotoxicity, which have promising practical potential [79]. In 2020, Wang *et al.* evaluated the biocompatibility of Fe_3O_4@PDA@BSA-Bi_2S_3 on mouse fibroblasts cells (L929). The viability of L929 cells was above 90% in all cases, confirming that materials less than 200 μg/mL can be used for biological applications [80]. Yuan *et al.* have evaluated the cytotoxicity of porous Co_3O_4 nanoplates (p-Co_3O_4 NPs) to both 4T1 cells and human melanoma cells (A375) (Fig. 3F) and confirmed 200 μg/mL as the LC10 for biological applications [81]. Similar to Group VIIIB transition metal oxides, an effective approach to prepare highly biocompatible POM-based nanoagents is to encapsulate POMs with cationic polymer. A series of reports of polymer-encapsulated POMs from Wu *et al.*, such as Mo_{154}@dendritic cation [82] and rPMo_{12}-soybean pentapeptide Ser-His-Cys-Met-Asn [83], exhibited low cytotoxicity on account of their precise chemical composition and definite molecular weight. In 2017, Cai *et al.* reported a redox-activated Ox-POM cluster for PAI-guided tumor ablation in response to the tumor microenvironment [84]. The *in vitro* toxicity of Ox-POM on human embryonic kidney 293 (HEK293) and 4T1 at different concentrations (0, 50, 100, 250, 500 μg/mL) was evaluated and found to be negligible for both cell lines even at high concentrations of 500 μg/mL. And it was also found that the ultrasmall Ox-POM clusters could escape recognition and capture by the liver and spleen, and were mainly excreted through the kidney, which is ideal for reducing the potential toxic effects caused by the long-term accumulation of nanoparticles in various organs and has important clinical prospects.

CTG luminescence cell viability Assay is a homogeneous method to determine the number of viable cells in culture based on quantitation of the ATP present, which signals the presence of metabol-

Table 1
Cytotoxicity of current reported transition metal oxide cluster-based nanomaterials.

Group	Transition metal oxide clusters	Cell type	Biological use preferable concentration	References
Group IVB	TiO_2/PEGDA NPs	HeLa	0.03 mol/L	[65]
Group	$W_{18}O_{49}$ NRs	MDA-MB-231	100 μg/mL	[66]
VIB	$W_{18}O_{49}$@LTN NRs	MDA-MB-231	200 μg/mL	[66]
(mostly	MoO_{3-x} QDs	HeLa	250 μg/mL	[85]
POMs)	D-/L-Cys-$MoO_{2.8}$	HeLa	200 μg /mL	[74]
	D-/L-Cys-MoO_2	HeLa	50 μg/mL	[74]
	D-/L-Cys-MoO_{3-x}	HeLa	200 μg/mL	[23]
	BSA-coated $Na_9[GdW_{10}O_{36}]$	HeLa	1000 μg/mL	[70]
	GdW_{10}@CS	human hepatocellular carcinoma cells (BEL-7402)	50 μg/mL	[86]
	nanosphere	HeLa	100 μg/mL	
	Garlic acid-reduced PW_{12}	4T1	200 μg/mL	[87]
	Reduced	rat renal proximal tubular cell line (NRK-52E)	500 μg/mL	[88]
	$[PMo_{12}]$	rat liver cell line (BRL)	500 μg/mL	
		MCF-7	500 μg/mL	
	Oxidized	4T1	500 μg/mL	[86]
	$[PMo_{12}]$	HEK293	500 μg/mL	
	TRIS-MnPOMo@SPB	HUVEC	200 μg/mL	[71]
	$(D\text{-}3)_{15}Mo_{154}$@DOXs	human hepatocyte cells (QSG-7701)	5000 nmol/L	[82]
	Mo_2C- POM	HUVEC	400 μg/mL	[89]
	Fe-doped-POM	HeLa	400 μg/mL	[90]
		HUVEC	500 μg/mL	
	$[Mo_{154}]$	HEK-293	50 μmol/L	[91]
	$[Mo_{154}]$ @VLPs			
Group	Ce6@MnO_2 -PEG	4T1	100 μmol/L	[67]
VIIB	BSA-MnO_2 NPs	HUVEC	300 mg/mL	[68]
		MCF-10A	300 mg/mL	
	MCPFNPs	MCF-7	200 μg/mL	[69]
		HeLa	200 μg/mL	
		NP69	200 μg/mL	
	MnO_2-SPs	4T1	600 μg/mL	[92]
	MONs@PDA-	LM3	50 μg/mL	[93]
	ICG	HepG2	50 μg/mL	
		SNU-387	50 μg/mL	
Group	Co_3O_4 NPs	U-87 MG	75 μg/mL	[94]
VIIIB	pCo_3O_4	4T1	200 μg/mL	[81]
	NPs	A375	200 μg/mL	
	PIONs	4T1	200 μg/mL	[76]
	Individual Fe_3O_4 NPs	A549	500 μg/mL	[79]
	Clustered Fe_3O_4 NPs	A549	500 μg/mL	[79]
	Fe_3O_4@PDA@BSA-Bi_2S_3	L929	200 μg/mL	[80]
Group	Lip(ASC/PFH)	MCF-7	20 μg/mL	[95]
IB,	UZNPs-PAA-DOX agents	L929	800 μg/mL	[73]
IIB	HMC-SS-ZnO	4T1	10 μg/mL	[72]

ically active cells, which has been widely employed for evaluation the cytotoxicity with higher sensitivity, faster detection and high accuracy than MTT and CCK8 assays. In 2018, Pan *et al.* used the standard CTG method to detect the potential cytotoxicity of PIONs on 4T1 cells. LC10 was reported to be 200 μg/mL for the biological application [76].

At the morphological level, bio-TEM can also be used to assess the internalization of different NPs and investigate the damage on cellular ultrastructures caused by NPs. To assess the toxicity of chiral MoO_{3-x} NPs on HeLa cells (Figs. 3E-A and 3E-B). Our group and co-workers reported that different L-Cys-and D-Cys-capped MoO_{3-x} NPs can internalize HeLa cells without significant damage to the cell membrane and ultrastructure. The membrane was structurally intact, and the cytoplasm was homogeneous without vacuum push. After crossing the cell membrane, the Cys-MoO_{3-x} NPs could aggregate into small clusters in the cytoplasm and the nanoparticles remained clearly visible. The evidence of bio-TEM can confirm their good biocompatibility suitable for biomedical applications [74].

In summary, the toxicity of transition metal oxides to various tumor cells (Hela cells, A375 cells, MCF-7 cells, 4T1 cells, human glioblastoma (U-87MG), *etc.*) is dose-dependent. Methods of modification, such as transition metal oxide nanoclusters capped with ligands [85], POMs encapsulated by cationic polymers are helpful to reduce the cytotoxicity [86–91]. Cytotoxicity of the same transition metal oxide cluster is almost identical to many tumor cell types [92–95]. For current reported transition metal oxide cluster, the average tolerance concentration was 200 μg/mL, as summarized in Table 1.

2.2. In vivo compatibility, biodistribution, main organs damages and clearance

Transition metal oxide cluster-based nanoagents were generally injected into tumor-bearing animals through both caudal vein and *in situ* tumor tissues. Therefore, investigation of the main organ damages, biodistribution and clearance ways of the nanoagents were essential for *in vivo* compatibility assessment, as the nanoagents can participate in the internal circulation and metabolism in the organisms.

Group VIB transition metal element, molybdenum, and tungsten oxide cluster-based nanoagents have been extensively studied in tumor phototherapy. Our group and coworkers have evaluated the *in vivo* compatibility of chiral Cys-capped MoO_{3-x} NPs. Immunohistological approach was employed to evaluate the main organ damages of mice after treatment (Fig. 4A-a). In addition, the biodistribution and metabolic pathways of chiral MoO_{3-x} NPs were

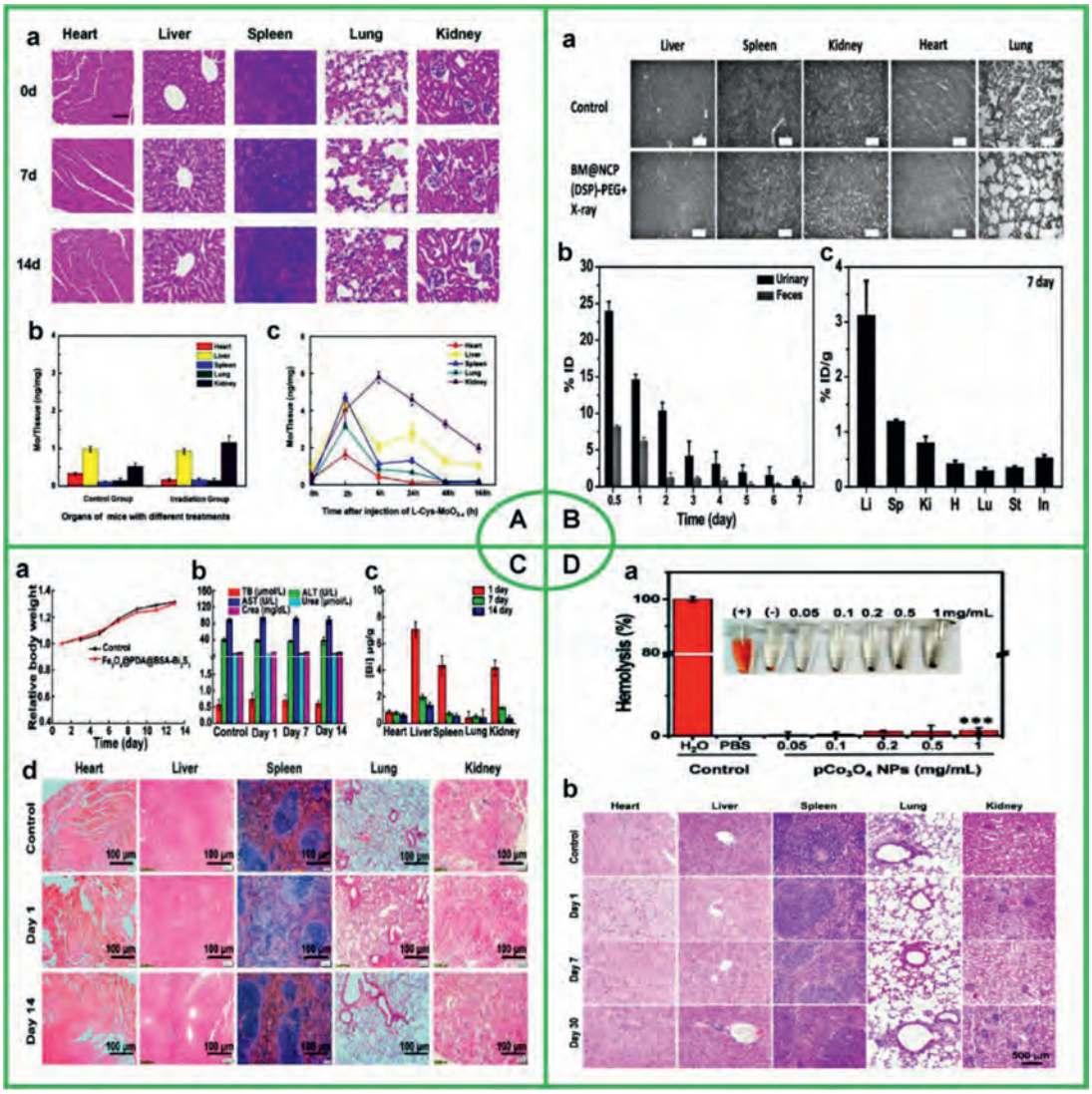

Fig. 4. *In vivo* compatibility evaluation of transition metal oxides. (A) Chiral MoO_{3-x} NPs. Reproduced with permission [23]. Copyright 2021, Elsevier. (B) BM@NCP(DSP)-PEG. Reproduced with permission [97]. Copyright 2017, Wiley-VCH Verlag GmbH & Co. KGaA. (C) Fe_3O_4@PDA@BSA-Bi_2S_3 NPs. Reproduced with permission [80]. Copyright 2020, American Chemical Society. (D) pCo_3O_4 NPs. Reproduced with permission [81]. Copyright 2020, Elsevier.

investigated by measuring Mo concentrations in main organs at selected time points after both intra-tumor (Fig. 4A-b) and intravenous injections (Fig. 4A-c). The results showed that the kidney peak occurs at 4 h and can be reduced to the lowest concentration in roughly 7 days, and that most chiral MoO_{3-x} agents can be rapidly cleared from the body, mainly from the kidney, without causing significant long-term toxicity [23]. Also, Liu *et al.* used the same approach to confirm the *in vivo* compatibility of MoO_{3-x} QDs and obtained similar conclusions [85]. The *in vivo* biocompatibility of the homologous tungsten oxide-based nanoagent, PEG-$W_{18}O_{49}$ NWs, was investigated by Hwang *et al*. indicating coating of PEG did not affect its metabolic pathway. Similar approaches were used to elucidate that the nanoagents is also metabolized mainly by the liver and kidney without damage to major organs [96].

Liu *et al.* developed a multifunctional nanocomposite, stabilized MnO_2@Nanoscale coordination polymers c,c,*t*-(diamminedichlorodisuccinato) Pt (IV) polyethylene glycol (BM@NCP(DSP)-PEG), which is mainly used for *in vivo* MRI-combined chemotherapy treatment. By H&E staining (Fig. 4B-a), they confirmed that the nanocomposite had no significant acute toxicity to animals. In addition, the concentration of hafnium (Hf) was measured by ICP-AES (Fig. 4B-b). After 7 days of injection, the level of Hf retained in the organs of mice was quite low (Fig. 4B-c), indicating that the nanoparticles were effectively cleared from the body [97]. For the case of BM@NCP(DSP)-PEG, the metabolic duration of a multiple complexed composite is affected by the interaction between various metal components and other constituents. The biodegradable nanocomposite has an effective excretory behavior. Fe_3O_4@PDA@BSA-Bi_2S_3 NPs, prepared by Wang *et al.* featured the synergistic treatment of PTT and chemodynamic therapy (CDT), with all conventional blood parameters, body weight and serum biochemical parameters within the normal range of the treated mice, indicating that the nanoagents were not harmful to the circulatory system *in vivo*. No damage to major organs was confirmed (Fig. 4C-d), while the element of Bi was metabolized mainly through the liver, reaching a peak at 24 h and decreasing to a minimum concentration at 14 days (Figs. 4C-a, b, c). It is evidenced that Fe_3O_4@PDA@BSA-Bi_2S_3 NPs have excellent biocompatibility, paving the way for their safe biomedical application [80].

Yuan *et al.* prepared pCo_3O_4 NPs for multimodal imaging (PA/MR imaging), and PDT/PTT synergistic phototherapy. They confirmed the hemocompatibility of pCo_3O_4 NPs (Fig. 4D-a), while pCo_3O_4 NPs did not damage major organs (Fig. 4D-b) [81]. Cai

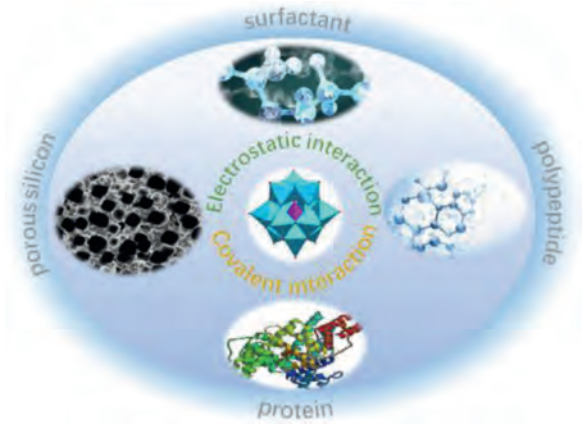

Scheme 1. Polypeptides, proteins, surfactants or porous silicon are employed to be linked with POMs by electrostatic or covalent interaction to improve their biocompatibility.

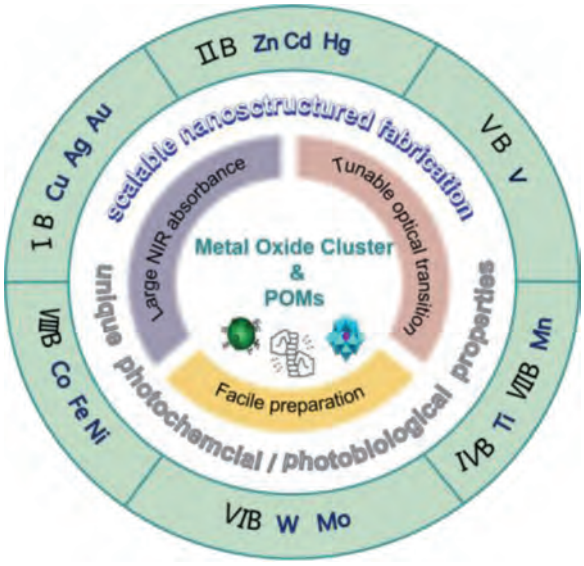

Fig. 5. Schematic illustration of physicochemical properties and current photosensitizing transition metal oxide cluster-based nanoagents.

et al. prepared Co_3O_4 NPs for photothermal treatment of tumors as well as *in vitro* combination therapy, and they obtained the same conclusion by a similar approach [94]. These work all confirmed that cobalt oxide-based nanoagents are biocompatible with potential medical applications.

In order to reduce the biotoxicity and improve biocompatibility of POM-based nanoagents, the strategy adopted was to enwrap POMs, which are mainly classified in electrostatic interactions and covalent interactions. As for electrostatic interactions, Wu *et al.* encapsulated POMs with positively charged biocompatible molecules, such as peptides [70,82,83,98,99], proteins [70,100,101], mesoporous silica [70], and cationic surfactants [102], as mentioned in "cyto-toxicity" section. Representative research of encapsulation of POMs by covalent interactions from Wei *et al.* [103,104], Lindqvist-type POMs grafted by a cleavable organoimido group was reported with its biodegradable property, leading to its low biotoxicity (Scheme 1).

To sum up, many transition metal oxide cluster-based nanoagents have exhibited the overall properties of low tissue toxicity and without damage to major organs after application. In addition, many of them also are biodegradable and eventually excreted, which indicates the superior biocompatibility, as well as prerequisite of practical applications.

3. Transition metal oxide cluster-based photosensitizer agents

Due to the beneficial physicochemical properties of biocompatibility and optical activities, transition metal oxide cluster-based nanostructures and their nanocomposites could serve as the suitable candidate for biomedical applications. Most of the transition metals also have a variety of valence states, which are able to form a variety of nanostructures with protonated terminal oxygen atoms, thus show massive special morphology, structures and photochemical properties. The various mechanisms for optical transition also promote multi-mode light-matter interactions in transition metal oxide cluster-based nanoagents, leading to the tunable and strong absorption in NIR range and facile preparation approach, transition metal oxide clusters have stood out as distinguished photosensitizing agents in nano-oncology applications (Fig. 5). In this section, we summarize and emphasize recent progress on the principle and research status of phototherapy based on transition metal oxide cluster-based nanoagents.

3.1. Late transition metal oxide nanoclusters

3.1.1. Group IB and IIB

The copper oxide is rarely used as optical material alone because of the low photothermal conversion efficiency. However, due to the low price and toxicity, copper oxides were widely employed as a component of photodynamic preparation of nanocomposites. In 2018, Liu *et al.* fabricated a unique Au@SiO_2@Cu_2O(ASC)-perfluorohexane (PFH) nanocomposite, in which the plasmonic ASC photosensitizer was loaded into the PFH nanodroplet coated with liposome Lip (ASC/PFH) [95]. By utilizing the plasmon-induced resonance energy transfer (PIRET) process from plasma Au to Cu_2O, ASC core-shell nanostructures show a higher $^1O_2$ production capacity under 670 nm laser irradiation than Cu_2O or Au@Cu_2O NPs. Due to its high oxygen capacity, PFH maintains a higher oxygen content than the tumor matrix at a given partial pressure of oxygen, providing oxygen enrichment for enhanced PDT and the presence of the silica layer ensures the nonradiative transfer of plasmonic energy from the Au NP core to Cu_2O. Under 670 nm laser irradiation, $^1O_2$ produced by Lip (ASC/PFH) caused the decrease of DPBF content and Calcein-AM and Propidium iodide (PI) staining results showed that 670 nm laser irradiation of Lip (ASC/PFH) treated MCF-7 cells generating a large amount of $^1O_2$ resulting in cell death due to PDT effect. *In vivo* study of MCF-7 bearing mice shows that the size of tumor of Lip (ASC/PFH) with irradiation group was minimum compares with other groups. The attractive self-enriched PIRET-PDT could serve as a promising platform for cancer treatment, which has significant implication in PDT design (Fig. 6A).

Zinc oxide has been reported as genotoxic drug to induce genetic-level damage and apoptosis of cells, which was mainly employed in anti-tumor PDT. The electrostatic properties of zinc oxide determine that the surface has different charges under specific conditions, which could be used for the bonding of therapeutic drugs. Meanwhile, due to the photodynamic properties of ZnO nanoclusters: light exposure leads to a large amount of ROS generation, which can lead apoptosis in cancer cell [105]. In 2020, Cai *et al.* have synthesized α-$NaYbF_4$:Tm@CaF_2:Nd@ZnO NPs by epitaxial growth method, and following with doxorubicin (DOX) loaded nanocomposites by polyacrylic acid (PAA) coating (names as UZNPs-PAA-DOX) [73]. The reasonable Yb^{3+}/Tm^{3+}/Nd^{3+} co-doping

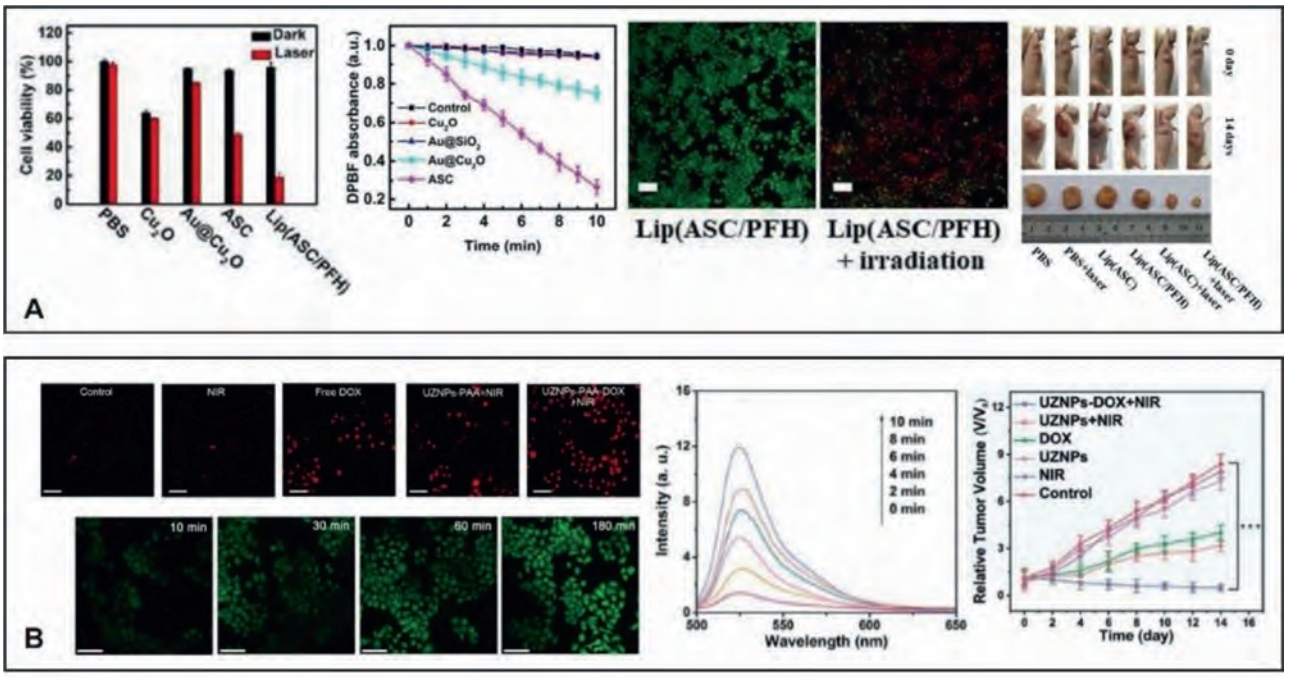

Fig. 6. Group IB and Group IIB metal oxide nanoclusters are applied in tumor diagnosis and therapeutics. (A) Group IB, Au@SiO_2@ Cu_2O. Reproduced with permission [95] . Copyright 2018, American Chemical Society. (B) Group IIB, UZNPs-PAA-DOX. Reproduced with permission [73]. Copyright 2020 American Chemical Society.

makes the nanoagents excited at 808 nm of NIR wavelength with low photo-damage and strong tissue penetration. CaF_2 could promote the luminescence intensity of clinical biological imaging as well as trigger electron hole pairs for PDT. The PAA was utilized to assemble DOX to form nanocomposite for photodynamic therapy and drug therapy. Due to the large number of hole electron pairs generated by ZnO, it could convert the surrounding water molecules and oxygen molecules into ROS. The color change of DCFH-DA in cells proved that the material could produce ROS in TME, which indicates that as-prepared NPs could improve the effect of PDT. In the same way, *in vivo* tumor inhibition experiments also showed that UZNPs-PAA-DOX nanomaterial has a good inhibitory effect on the tumor model due to the PDT effect (Fig. 6B).

3.1.2. Group VIIIB

Iron oxide-based nanoagents feature multiple valence states and could be combined with oxygen in various forms. Thanks to its high optical activity as well as magnetic properties, the iron oxides could be used for magnetothermal therapy and combined MRI to treat tumors. For instance, Fu *et al.* fabricated the superparamagnetic Fe_3O_4 NPs [106]. The as-prepared superparamagnetic NPs exhibited light absorption in the visible and NIR and could convert light into heat. The heating conversion experiment showed that the photothermal effect is both concentration- and laser intensity- dependent. Tumor cell ablation study showed that after irradiation guided by NPs, the 4T1 tumor cell activity decreased to 50%, and further decreased to 24.1% after external magnetic field was applied. Furthermore, Barrera *et al.* fabricated an iron-based nanocomposite for photothermal therapy and bioimaging [107], which is composed of reduced graphene oxide (rGO) nanosheets as the photothermal agent and iron oxide (Fe_3O_4) NPs formed *in situ* to provide magnetic properties used for MRI. Under 804 nm irradiation, the temperature of rGO-Fe_3O_4 rapidly increased by around 18 °C, manifesting its potential photothermal effect. *In vitro* irradiation experiments showed that the survival rate of HeLa cells treated with 50 μg/mL NPs was only 32.6%. However, the survival rate of cells treated by laser alone was 83%, reveals the enhanced cancer-cell-killing efficacy of rGO-Fe_3O_4 due to its high photothermal conversion ability. In 2018, Hu *et al.* synthesized multifunctional porous iron oxide nano-agents (PIONs) for combined photothermal/chemotherapy [76]. This porous structure, composed of smaller iron oxide particles, have relatively large specific surface area which is favorable for loading of DOX hydrochloride. The modification of polyacrylamide (PAM) not only makes the PIONs have better solubility and biocompatibility, but also can prevent the Fe_3O_4 from being oxidized to Fe_2O_3, thus obtaining a more stable photothermal ability. *In vitro* study shows that the survival rate of 4T1 cells was 60% after laser irradiation alone and can be further reduced to 25% when combined DOX and laser irradiation, indicating that the PIONs nanocomposite has the ability to guide synergistic efficient effect of PTT and chemotherapy (Fig. 7A). In 2020, Luo *et al.* created a novel Fe_3O_4@PDA@BSA-Bi_2S_3 composite as a therapeutic agent [80]. Fe_3O_4 NPs could work as a mimetic peroxidase to trigger Fenton reaction and produce ·OH to induce tumor cells apoptosis. On the other hand, it can be used as MRI contrast agent to provide precise cancer diagnosis. PDA could prevent oxidation of Fe_3O_4 to keep the long-term Fenton reaction. The Bi_2S_3 component exhibits excellent photothermal transducing performance and CT imaging capacity owing to the X-ray attenuation of Bi atoms. Under 808 nm laser irradiation, the ΔT remains constant during 10 consecutive laser on/off cycles, proving that the heat production would not attenuate after multiple irradiations. *In vivo* study showed that the tumor of nude mice bearing HT29 which injected Fe_3O_4@PDA@BSA-Bi_2S_3 NPs with laser irradiation was inhibited obviously due to the PTT and CDT indicating its potential diverse application prospects in biomedicine (Fig. 7B).

According to the previous reports, the multifunctional cancer therapeutic agents also involved “intelligent” nickel oxide NPs (NOP). In 2016, Bano *et al.* fabricated the core-shell NPs for combined chemo and photodynamic cancer therapy [108]. They loaded traditional anticancer drug DOX on the surface of water-dispersible NOPs *via* electronic interactions and then constructed the BSA shell through the cross-linking procedure. NOPs were capable of loading high amount of DOX, and BSA shell facilitated in cancer cell

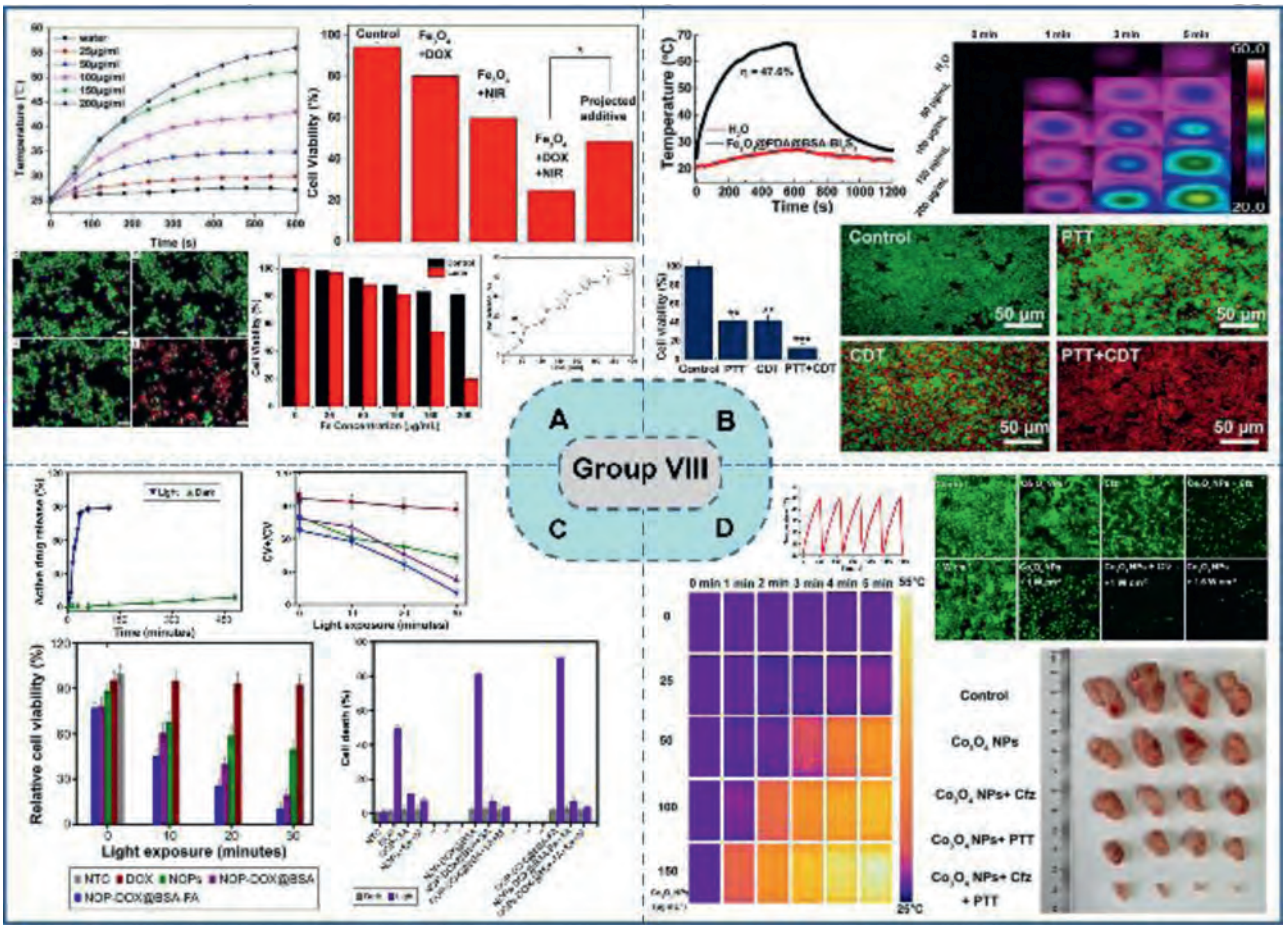

Fig. 7. Group VIII elements oxides in tumor application. (A) PIONs. Reproduced with permission [76]. Copyright 2018, American Chemical Society. (B) Fe_3O_4@PDA@BSA-Bi_2S_3. Reproduced with permission [80]. Copyright 2020, American Chemical Society. (C) NOP-DOX@BSA-FA. Reproduced with permission [108]. Copyright 2016, Dove Press. (D) Co_3O_4 NPs. Reproduced with permission [94]. Copyright 2021, Elsevier.

targeting and preventing drug leakage during transit to the target sites. This nanomaterial greatly improves the efficiency of drug delivery, and more importantly, its photodynamic effects also contribute to future clinical application prospects. Irradiation experiment is employed in investigating the cell apoptosis rate guided by NOP-DOX@BSA-FA on HeLa cell, the difference of over 70% of the cell viability indicates that laser can significantly stimulate the photodynamic reaction guided by NOPs, which produced ROS, oxidizing tumor cells and inducing their apoptosis (Fig. 7C).

The applications of cobalt oxide nanomaterials in phototherapy have been reported in recent years. In 2020, Huang *et al.* synthesized multifunctional Co_3O_4 nanoparticle to enhance anti-cancer therapeutic [94]. The prepared Co_3O_4 NPs can improve the efficiency of anticancer treatment by manipulating the protein degradation pathway and induce autolysosome accumulation and lysosome function damage. Meanwhile, because of its high photothermal conversion efficiency, the efficacy of anti-tumor therapy can be enhanced through the photothermal effect. The *in vitro* irradiation experiment results showed that the temperature increased rapidly in a dose-dependent manner, and there was no temperature decreasing in five cycles, which indicated its photothermal conversion stability. *In vivo* irradiation study carried out on glioblastoma cell bearing mice showed that during the PTT guided by Co_3O_4 NPs, tumor tissue temperature can rise to 47 °C within 2 min. Compared with control group, the tumor volume of experimental group was significantly reduced, indicating an effective tumor inhibiting ability, which also indicates the PTT application prospect (Fig. 7D).

3.2. Early transition metal oxide clusters (mostly POMs)

3.2.1. Group VIB (polyoxomolybdates, polyoxotungstates and other nanoclusters)

Molybdenum, featuring variable oxidation states, is an essential trace element and nutrient that is necessary for the survival of all living body [109–112]. Mo oxide clusters has been proven to be able to treat cancer on account of their good NIR photothermal conversion efficiency and inhibition of enzymes [113], inducing caspase-dependent and mitochondria-mediated apoptosis. Pioneering research related to polyoxomolybdate-based PDT agents from Lee *et al.* described that photosensitizer complexed with POMs can realize the increase of PDT activity due to the enhanced delivery system of POM complex [114,115]. Shi's group firstly developed naked polyoxomolybdates, a series of reduced keggin-type POMs, identifying that reduced [PMo_{12}] can change its dimension from small (1 nm) to big (tens of nanometer) [88], which is consistent with the discovery from Liu *et al.* [116,117]. When being reduced, color of polyoxomolybdate solution turns from salmon subsequently to jasper then to montana, and the absorption of the solution undergoes a red shift. In the case, reduced [PMo_{12}] demonstrated a previously unrealized tumor-specific photo-hyperthermia, combined with their favorable intratumoral accumulation. Similarly, Cai *et al.* reported PAI-guided tumor ablation of the oxidized [PMo_{12}] in 4T1 tumor-bearing mice subsequently. A giant polyoxomolybdates, Mo_{154}, wrapped by triethylene glycol monomethyl ether terminal groups-containing cationic dendrons by a simple

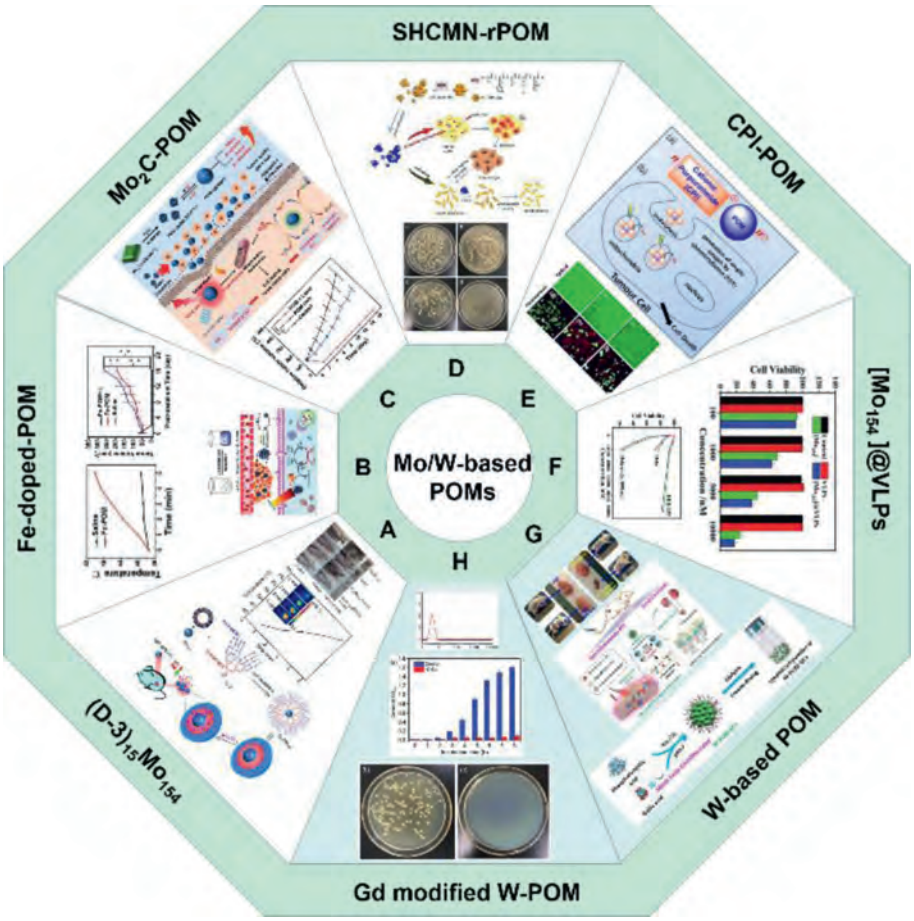

Fig. 8. Application of POM-based phototherapeutic nanoagents. (A) $(D\text{-}3)_{15}Mo_{154}$. Reproduced with permission [82]. Copyright 2018, the Royal Society of Chemistry. (B) Fe-doped-POM. Reproduced with permission [90]. Copyright 2020, Wiley-VCH Verlag GmbH & Co. KGaA. (C) Mo_2C-POM. Reproduced with permission [89]. Copyright 2020, Wiley-VCH Verlag GmbH & Co. KGaA. (D) SHCMN-rPOM. Reproduced with permission [83]. Copyright 2019, the Royal Society of Chemistry. (E) CPI-POM. Reproduced with permission [115]. Copyright 2018, Wiley-VCH Verlag GmbH & Co. KGaA. (F) $[Mo_{154}]$@VLPs. Reproduced with permission [91]. Copyright 2021, the Royal Society of Chemistry. (G) W-based POM. Reproduced with permission [87]. Copyright 2020, American Chemical Society. (H) Gd modified W-POM. Reproduced with permission [99]. Copyright 2021, The Royal Society of Chemistry.

electrostatic interaction, reported by Wu *et al.* (Fig. 8A) [82]. As-prepared nanocomposites, $D_{15}Mo_{154}$ complex, exhibited monodispersion and low cytotoxicity, with imparted loading of anticancer drug, DOX, and thermoresponsive properties. For Mo-based POMs, a multifunctional Fe-doped Mo-based polyoxometalate cluster has been developed, which can not only be used as a photothermal conversion agent in NIR-II laser irradiation to produce thermal effect to kill cancer cells, the Fe^{2+} and Mo^{5+} in Fe-POM can also destroy tumor tissue by converting H_2O_2 at the tumor site into the more toxic ·OH through Fenton reaction. Fe^{3+} and Mo^{6+} produced by the reaction can further react with GSH in the environment, leading to the decrease of GSH content in tumor micro-environment, thus destroying its antioxidant defense system and further killing tumor. In the neutral environment with pH of 7.4, the particle size of Fe-POM clusters was 12.9 nm. When pH decreased to 6, the cluster size increased to 271.1 nm due to the formation of hydrogen bonds induced by protonation in acidic environment, which made it better to exist in tumor tissues. *In vitro* and *in vivo* experiments have proved its good killing ability of tumor cells, providing a new nano platform for the enhancement of CDT by PTT in NIR-II biological window (Fig. 8B) [90]. What is more, a Mo_2C-derived POM was synthesized as a new CDT agent (Fig. 8C) [89]. The prepared reagents can achieve PAI-guided CDT and PTT to kill tumor cells. Acid-induced aggregation enables Mo-POM to specifically target tumor tissue, aggregate at the tumor site, and enhance NIR absorption, thus achieving tumor cell ablation. It was found that Mo-POM produced $^1O_2$ during CDT, probably through Russell mechanism rather than Fenton reaction. Furthermore, Zhang *et al.* prepared a polyoxometalate (r-POMS) cluster modified by soybean pentapeptidase (SHCMN) through molecular interaction. SHCMN, as an antioxidant, cannot only enhance its physiological stability, but also enhance the bactericidal effect caused by photothermal effect (Fig. 8D) [83]. The reducing solution (rSP) was obtained by UV irradiation of the co-assembled clusters for 5 min. During the irradiation process, the color of the solution changed from yellow to dark blue. The rSP exhibits spherical aggregates of 60 nm due to electrostatic and hydrogen bonding and exhibits obvious absorption in the NIR. It can be used in NIR-triggered PTT due to the intervalence electron transfer of Mo^{6+} into Mo^{5+}. In addition, Tae Heon Lee *et al.* synthesized cationic purpurinimides (CPIs) derivatives, such as ammonium, pyridinium and pyridinium salts, and then used them to prepare CPIs-POM supramolecular complexes, showing long-wavelength absorption (λ_{max} = 707 nm) and cellular uptake, followed by mitochondrial targeting to induce mitochondrial light-mediated apoptosis of tumor cells (Fig. 8E) [115]. It was found that the prepared CPIs exhibited concentration-dependent dark cytotoxicity, while CPIs-POM showed a significantly reduced dark cytotoxicity, making it a potential candidate for photosensitizer for PDT. Due to the presence of POM, CPIs-POM showed enhanced PDT effect under 707 nm

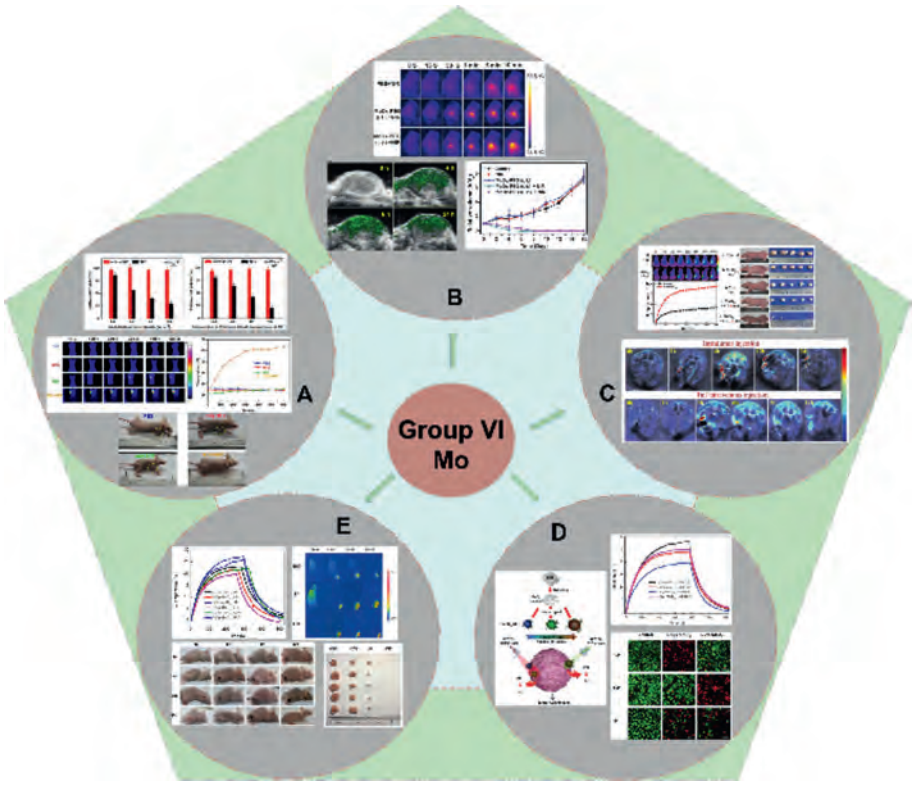

Fig. 9. Group VI elements oxides in tumor application. (A) C/MoO_2. Reproduced with permission [121]. Copyright 2012, the Royal Society of Chemistry. (B) PEG-MoO_{3-x} nanosheets. Reproduced with permission [122]. Copyright 2015, Wiley-VCH Verlag GmbH & Co. KGaA. (C) MoO_{3-x} QDs. Reproduced with permission [85]. Copyright 2017, the Royal Society of Chemistry. (D,E) Chiral MoO_{3-x}. Reproduced with permission [74]. Copyright 2019, Wiley-VCH Verlag GmbH & Co. KGaA. Reproduced with permission [23]. Copyright 2021, Elsevier.

laser irradiation and showed significant PDT killing effect on A549 and HeLa cells.

In addition to POMs based on Mo, POM based on W has also been reported [118–120]. For example, Zhou *et al*. prepared W-based POM NCs through a facile redox reaction with natural gallic acid in an alkaline aqueous solution (Fig. 8F) [91]. It presents a monodisperse and uniform spherical structure with an average diameter of 2.0 nm. W-POMs NCs show excellent stability in the form of freeze-dried powder. *In vivo* and *in vitro* experiments show that its good biocompatibility, not only shows obvious NIR absorption capacity to achieve photothermal treatment, but also oxidizes W^{5+} to W^{6+} eliminates ROS associated with inflammation and thus exhibits an impressive anti-inflammatory effect. Apart from above, a novel food-derived antioxidant peptide with high free radical scavenging ability identified from the hydrolysates of trepang protein was assembled with Gd modified $Na_9GdW_{10}O_{36}{\cdot}18H_2O$ through supramolecular interaction to form a supramolecular complex (K-Gd) in 2021 (Fig. 8G) [87]. Under physiological conditions, K-Gd maintains uniform ultra-small particle size and excellent biocompatibility. The results show that the prepared K-Gd has good MRI and CT performance and has good photothermal sterilization effect. The supramolecular complex platform has potential for accurate early medical diagnosis and effective eradication of tumor cells (Fig. 8H) [99].

Bioactive Mo-based oxides with different Mo valent states include stoichiometric molybdenum dioxide (MoO_2), molybdenum trioxide (MoO_3) and sub-stoichiometric molybdenum oxide (MoO_{3-x}, also known as mixed valence molybdenum oxide). Due to these enriched oxygen vacancies during redox preparation, MoO_{3-x} has strong LSPR in the NIR, it could be utilized as ideal PTA agents in the cancer therapy. However, MoO_2 and MoO_3 do not exhibit LSPR, which can be obtained by adjusting their structures or modifying them with other substances. In addition, although MoO_{3-x} exhibits LSPR, it will lose the ability of LSPR as oxygen gradually filling the vacancies. Therefore, it is very important to find a desirable strategy to improve the stability of MoO_{3-x}. For oxide-based nanostructure, ultra-thin carbon-coated MoO_2 hybrid NPs (C/MoO_2) has been reported since several years ago. In 2012, Liu *et al.* prepared uniformly aggregated C/MoO_2 with diameters ~120 nm by an easy-solvent thermal method [121]. The carbon layer of 1–2 nm is tightly wrapped around the surface of individual MoO_2 NPs, which effectively prevents the massive aggregation of MoO_2 NPs. The surface of C/MoO_2 NPs was then modified with sulfhydryl-functionalized polyethylene glycol (SH-PEG) to improve their biocompatibility. Due to the strong NIR absorption and great stability in physiological solutions, C/MnO_2 NPs with PEGylation have efficient PTA on cancer cells. *In vitro* and *in vivo* experiments have shown that cancer cells cultured with NPs (1 mg/mL) can be effectively killed after being irradiated with an 808 nm near-infrared laser for 5 min, with a power density of 0.6 W/cm^2. The results suggested that the new C/MoO_2 NPs can be used as promising NIR photothermal agents to induce local higher temperature for burning tumors (Fig. 9A). The 2D MoO_{3-x} nanosheets functionalized with PEG has been reported recently [122]. It serves as both the degradable PTA agent and drug carrier. The experimental outcomes confirmed the rapid biodegradation of nanocomposites after intravenous injection. In addition, the strong absorption in NIR range also made MoO_{3-x} contrast PAI agent, which rapidly monitors *in vivo* degradation in muscles (Fig. 9B). Moreover, in 2017, Ding *et al.* fabricated a multifunctional therapeutic system using MoO_{3-x} quantum dots (QDs), which can realize PAI guided dual-therapy (PDT/PTT) for cancer treatment [85]. The MoO_{3-x} QDs show strong optical absorption in biological window and a high photothermal conversion efficiency. Apart from this, the singlet

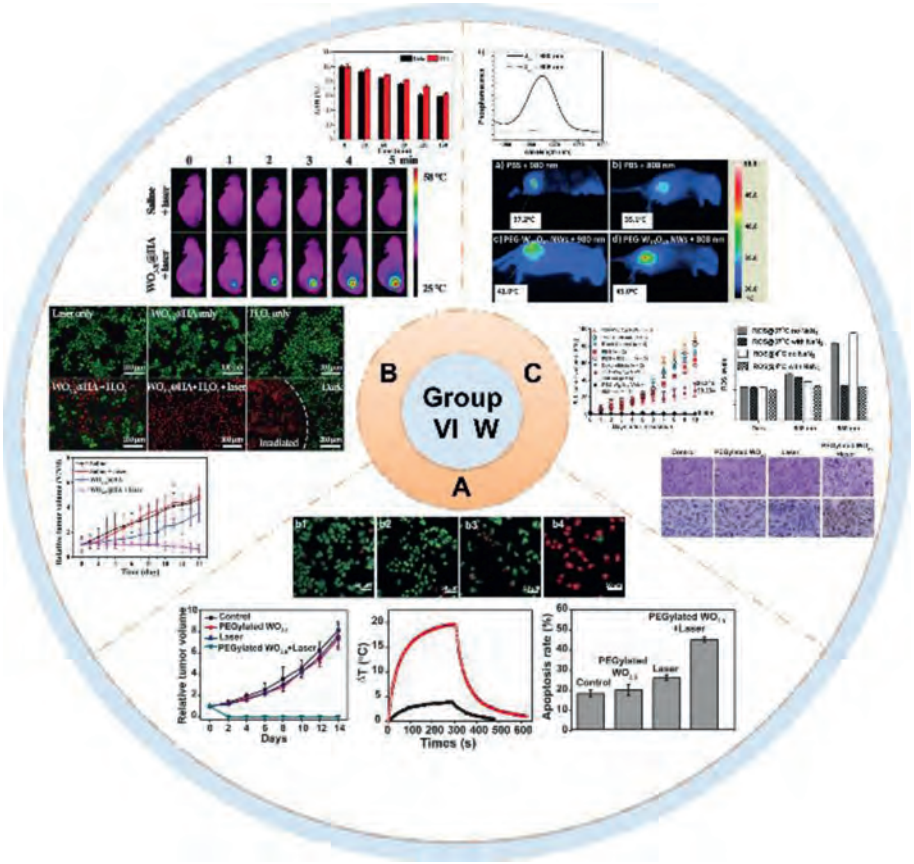

Fig. 10. Group VI tungsten oxides in tumor application. (A) PEG-$WO_{2.9}$ NRs. Reproduced with permission [24]. Copyright 2017, Nature Publishing Group. (B) WO_{3-x} @HA. Reproduced with permission [126]. Copyright 2021, the Partner Organisations. (C) PEGylated $W_{18}O_{49}$ NWs. Reproduced with permission [96]. Copyright 2013, Wiley-VCH Verlag GmbH & Co. KGaA.

oxygen also could be generated simultaneously by MoO_{3-x} QDs for executing dual-therapy of PTT/PDT under NIR 880 nm irradiation. In addition, by increasing the laser power density and the concentration of MoO_{3-x} QDs, the photo-destruction of HeLa cells can also be enhanced. The photodamage of tumor cells can be explained by heat diffusion and ROS migration-induced lysosomal damage and cytoskeletal protein degradation. A living imaging study showed that MoO_{3-x} QDs also could be employed as a PAI contrast agent owing to the excellent photothermal conversion ability (Fig. 9C). Furthermore, taking advantage of their unique plasmonic behavior, Xu *et al.* prepared a kind of strong nonstoichiometric molybdenum oxide nanomaterial with visible and near-infrared dual channels by a chiral induction effect [23,74]. Its selective optical absorption characteristics make it a more efficient photothermal agent under chiral light illumination, which can be applied in PTT of cancer cells [123]. By redox reactions adjustment, controllable chiral molybdenum oxide NPs with a visible or NIR range were synthesized. The tunable valent states chiral molybdenum oxide NPs with different optical properties can be prepared by a simple wet chemical method [124]. The as-prepared chiral NPs not only have strong selective absorption in the conventional NIR by LSPR but also have emerged the strong visible light region (300–700 nm) chirality resulted by the metal ligand charge transfer (MLCT) [125]. These characteristics provide a new approach for the application of this material in the photothermal treatment of cancer cells. Its main characteristics include the following: (1) The asymmetric factors in the solution state can reach 10^{-3} orders of magnitude in the metal ligand charge transfer region; (2) Compared with traditional molybdenum oxide PTT agents, higher photothermal conversion efficiency and higher cancer cell lethal efficiency are achieved; (3) In addition to being traditional NIR PTT agents, the material can also work in the visible light region, which will provide a new approach for the treatment of skin cancer cells (Figs. 9D and E).

Tungsten oxide clusters is a class of versatile transition metal oxides with a large number of polycrystalline and substoichiometric components, featuring oxygen vacancies. The structure determined property, such as altered optical absorption makes tungsten oxide an attractive candidate for phototherapy. For example, In 2014, Zhou *et al.* prepared tungsten oxide($WO_{2.9}$)NRs for tumor diagnosis [24]. $WO_{2.9}$ NRs were coated with PEG *via* ligand exchange to obtain a better water dispersability and biocompatibility. They injected PEG-$WO_{2.9}$ NRs dispersed in normal saline into HeLa tumor-bearing mice at a dose of 20 mg/kg and found that the tumor CT signal was significantly enhanced immediately after injection (235 ± 30 HU to 6996 ± 1735 HU). After PEG-$WO_{2.9}$ NRs entered into tumors tissues through EPR effect, it was irradiated by a 980 nm laser at 0.35 W/cm^2 for 5 min, irradiation results showed that the temperature of the tumor rapidly increased by 20 °C which could kill the tumors *in vivo*. In contrast, injection of non-PEG $WO_{2.9}$ NRs had no significant effect on tumor temperature. Therefore, PEG-$WO_{2.9}$ NRs could also be feasible to serve as photothermal agent *in vivo* (Fig. 10A). What is more, Ding *et al.* developed WO_{3-x}@HA with full-spectrum absorption characteristics [126]. Researchers selected 1064 nm laser to study photothermal conversion characteristics and monitored the process with an infrared thermal imager, during which the NPs aqueous solution showed an efficient temperature rise. This indicates that oxygen vacancies in WO_{3-x} launch strong LSPR absorption to realize the efficient NIR-II photothermal conversion. The time-dependent tem-

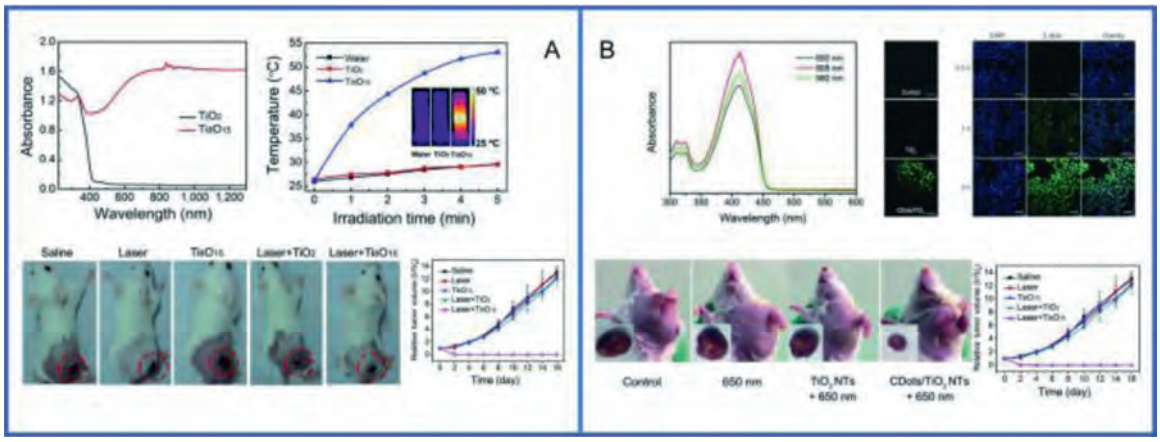

Fig. 11. Group IVB metal oxide nanoclusters in PTT. (A) Ti_8O_{15} NPs. Reproduced with permission [127]. Copyright 2016, Springer. (B) C dots/TiO_2 NTs. Reproduced with permission [128]. Copyright 2018, Wiley-VCH Verlag GmbH & Co. KGaA.

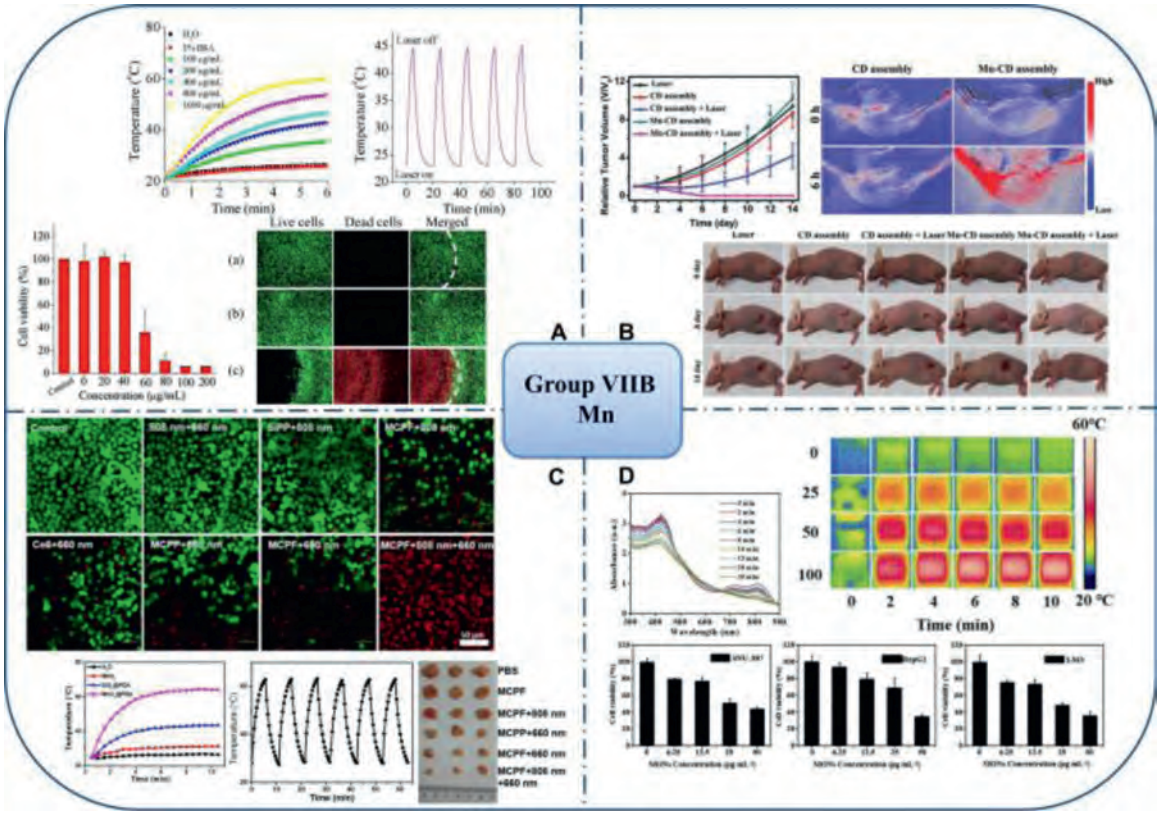

Fig. 12. Group VII elements oxides in tumor application. (A) BSA-MnO_2 NPs. Reproduced with permission [68]. Copyright 2018, Elsevier. (B) MnO–CDs. Reproduced with permission [130]. Copyright 2018, Wiley-VCH Verlag GmbH & Co. KGaA. (C) MCPF NPs. Reproduced with permission [69]. Copyright 2020, Elsevier. (D) MONs@PDA-ICG. Reproduced with permission [93]. Copyright 2021, Frontiers Media S.A.

perature curve of WO_{3-x} suggests that the photothermal conversion efficiency is 43.6%. Therefore, WO_{3-x} @HA can be used as a NIR-II photothermal agent to convert NIR-II radiation quickly and effectively into heat energy (Fig. 10B). Furthermore, PEG-$W_{18}O_{49}$ nanomaterials have realized strong PDT effects [96]. Kalluru *et al.* used two different wavelengths of laser (808 nm and 980 nm) to irradiate HeLa cells. The number of photons absorbed by PEG-$W_{18}O_{49}$ nanowires (NWs) at 808 nm and 980 nm identical. When using a higher light intensity, more cell death was observed with internalization of PEG-$W_{18}O_{49}$ NWs. It is widely accepted that the PEG-$W_{18}O_{49}$ NWs can sensitize the formation of singlet oxygen under 980 nm light but not under 808 nm light. Therefore, the cell death induced by 808 nm laser irradiation might be the result of photothermal heating, and the PDT effect mediated by singlet oxygen is the only controlling factor of cell death induced by 980 nm light irradiation. The content of ROS in HeLa cells pretreated with and without sodium azide (NaN_3) was determined. NaN_3 is a specific scavenger of singlet oxygen, so when ROS come from singlet oxygen, it can reduce the level of ROS in cells. Therefore, this work also suggested that the amount of ROS generated by 980 nm light irradiation is much higher than 808 nm light irradiation (Fig. 10C).

3.2.2. Group VB (polyoxovanadates)

Gu *et al.* designed and synthesized the supramolecular assemblies based on polyoxovanadate anions and iodobodipy cations for photochemotherapy [104]. The iodobodipy cation has the ability to

photogenerate $^1O_2$, and the polyoxovanadate anion has potential anticancer activity (including chemotherapy and PDT), so the prepared (2I-BDP-C_6)$_3V_{10}$ can be used for photochemical therapy. This work will provide a new way to expand the use of POV in cancer treatment.

3.2.3. Other early transition metal clusters (IVB and VIIB)

Titanium oxide, a wide band gap semiconductor optical material, has been widely used in phototherapy due to its excellent light energy conversion efficiency, strong oxidation and nontoxic properties. In 2016, Ou *et al.* synthesized Magnéli-phase Ti_8O_{15} NPs by the arc-melting technique [127]. Compared to the traditional TiO_2 materials, the Ti_8O_{15} NPs have high NIR absorbance and high photothermal conversion efficiency. 4T1 cells were co-incubated with 0.125 mg/mL Ti_8O_{15} NPs and TiO_2 NPs respectively for 24 h, and then irradiated with 808 nm laser for 5 min. The dead cells were distinguished from the living cells by trypan blue staining, and MTT assay was used to evaluate the cell activity after PTT. The results showed that with the increase of laser intensity, the survival cells gradually decreased, while the cells in the TiO_2 treatment group showed almost no photothermal ablation effect. *In vivo* study shows that after laser irradiation of the tumor tissue in mice injected with Ti_8O_{15} NPs, the local tumor temperature rose to 60 °C within 5 min, which was significantly higher than that in saline and TiO_2 treatment groups, and the tumor volume in this treatment group was significantly lower than that in other treatment groups, indicating the strong tumor inhibition ability of Ti_8O_{15} NPs (Fig. 11A).

ROS are substances with high oxidation potential, which mainly damage DNA and cell membrane of cancer cells. TiO_2 NPs excited by ultraviolet light (UV) are the source of active oxygen formed on their surface. However, the limited penetration of UV radiation to tissues seriously hindered the application of TiO_2 UV sensitized NPs in tumor-targeted phototherapy. In order to solve this problem, Yang *et al.* fabricated a kind of carbon-nanodot-decorated TiO_2 nanotubes (C dots/TiO_2 NTs) [128] composite which could be excited by 650 nm near infrared light, thus greatly improved the tissue penetrating ability and could be used for PDT *via* the stepwise water-splitting process: (i) $2H_2O \rightarrow H_2O_2 + H_2$; (ii) $2H_2O_2 \rightarrow 2H_2O + O_2$. Significantly, the relative position of the C Dots band edge permits the electron transfer from the surface of TiO_2 materials, which allows the separation, stabilization, and hindered recombination of electron/hole pairs, account for the higher activity of this photosensitizer. Moreover, the DCFH-DA probe evaluation of its ROS production capacity showed that carbon-modified TiO_2 was much higher than that of unmodified TiO_2. *In vitro* study showed that the mortality of tumor cells treated with NTs was 80% after being exposed to 650 nm laser for 10 min. Similarly, *in vivo* study showed that the tumor growth of tumor-bearing mice treated with NTs and laser irradiation was significantly inhibited, indicating its favorable PDT ability (Fig. 11B).

On the other hand, with the development of sonodynamic therapy (SDT) method, more effective and stable sono-sensitizers are developed, which allows the production of ROS in deeper tissues. Recently, Wang *et al.* fabricated ultrafine titanium monoxide nanorods (TiO_{1+x} NRs) with greatly improved sono-sensitization and Fenton-like catalytic activity for enhanced SDT [5]. Compared to conventional TiO_2 NPs, TiO_{1+x} NRs can also be used as a Fenton-like agent to generate highly toxic ·OH for CDT-induced cancer killing due to Ti^{3+} presence. What is more, The NRs can achieve efficient SDT/CDT for tumor elimination after intravenous injection under UV irradiation and are much more effective than TiO_2 NPs. We suppose SDT, CDT and PDT could be combined to generate more ROS and induce apoptosis of cancer cells, so as to achieve more efficient anti-tumor effect.

Manganese dioxide nano drug delivery system is widely combined with tumor PDT to achieve the purpose of tumor clearance in recent years [129]. For the hybrid nanostructures, Liu *et al.* fabricated BSA-MnO_2 NPs through a facile one-step route utilizing BSA as both template and reducing agent [68]. The BSA coating also contributes high water dispersibility, good biocompatibility as well as colloidal stability in different physiological environments to MnO_2 based NPs. Due to the superior NIR photothermal efficiency and photostability of the BSA-MnO_2 NPs, it has become a novel class of photothermal antitumor agent. To investigate their localized anti-tumor PTT ability, study on A549 was carried. After exposure to 810 nm laser, the cells incubated with 40 μg/mL BSA-MnO_2 NPs solution kept survival. In contrast, after treated with BSA-MnO_2 NPs with laser exposure, cells within the laser spot were substantially killed while most cells outside retained survival, suggesting that BSA-MnO_2 NPs could mediate localized hyperthermia to ablate the cancer cells *in vitro* (Fig. 12A). In 2018, Jia *et al.* prepared magnetically fluorescent MnO–CDs derived from manganese(II) phthalocyanine (Mn-Pc) and then self-assembled them in collaboration with DSPE-PEG to improve water solubility and biocompatibility [130]. The carbon dots (CDs) can efficiently generate $^1O_2$ for PDT and promote MnO–CDs assembly to obtain better performance in exhibiting physiological stability, NIR emission and efficient $^1O_2$ generation. More importantly, MnO–CDs components can highly catalyze H_2O_2 producing oxygen and successfully improving tumor hypoxia and PDT efficiency. *In vitro* and *in vivo* studies have shown that the magnetically fluorescent MnO–CDs module could be used as an acid H_2O_2-driven oxygen generator for bimodal fluorescence imaging (FLI) and MRI, which effectively improves PDT efficacy in anoxic solid tumors through *in situ* oxygen generation (Fig. 12B). In addition, in 2020, Zeng designed a multifunctional nanoplatform formed by hollow mesoporous MnO_2 NPs encapsulating the chlorin e6(Ce6) and also further coated with folic acid-functionalized polydopamine (PDA) (MnO_2@Ce6@PDA-FA NPs, MCPF NPs) [69]. Ce6 is a kind of photosensitizer which possesses a strong singlet oxygen generation capacity and PDA film could prevent the leakage of the drug in blood circulation. Further, the nanoplatforms specifically release Ce6 in response to endogenous stimuli (H^+ and/or H_2O_2 in TME) and/or external stimuli (laser). Specifically, PDA shell structure disintegrates in acidic environment, exposing MnO_2 core structure, which reacts with H_2O_2 to produce more O_2 to accelerate the release of Ce6. The $^1O_2$ production alleviates the hypoxia of tumor tissue and greatly promotes the PDT reaction triggered by 660 nm laser irradiation. *In vivo* study shows that the tumor temperature in the MCPF with 808 nm laser irradiation group of 4T1 tumor-bearing mice rose to 44.1 °C within 5 min. What is more, the anti-tumor effect of two wavelengths (808 nm and 660 nm) laser treating group was more obvious than that other, indicating that MCPF NPs can provide a novel and efficient anti-tumor phototherapy by synergistic PDT and PTT effects (Fig. 9C). In 2021, Zhu *et al.* constructed a nanoscale therapeutic agent (MONs@PDA-ICG) with manganese oxide nanoflowers (MONs) as the core, PDA as the shell, and indocyanine green (ICG) as the photosensitizer and photothermal agent for the synergistic treatment of liver cancer by TME-responsive MRI and PDT/PTT [93]. Under 808 nm laser irradiation, MONs@PDA-ICG can not only produce ROS to kill cancer cells, but also show good photothermal properties. At the same time, MONs@PDA-ICG releases oxygen and Mn^{2+} ions in the TME. The oxygen produced alleviates the hypoxia of the tumor and further enhances the therapeutic effect of PDT. In addition, the release of Mn^{2+} ions make MONs@PDA-ICG a TME-responsive MRI contrast agent for highly sensitive and specific diagnostic of liver cancer. This remarkable therapeutic effect has been demonstrated in representative (hepatocellular carcinoma) HCC cells lines, including human hepatocellular carcinoma (HCC) cell lines (LM3, HepG2, SNU-387). These findings support

Table 2
A summary of transition metal oxide cluster-based phototherapy agents and applications in this review.

Transition mental group	Materials	λ (nm)	η	Applications	Tumor-model	Ref.
IVB	Ti_8O_{15}	808		PTT	4T1	[127]
	C dots/TiO_2 NTs	650		PDT	U41	[128]
VB	$(2I\text{-}BDP\text{-}C_6)_3V_{10}$	550		PDT		[104]
VIB	C/MoO_2	808		PTT	MDA-MB-231	[121]
	MoO_{3-x} Nanosheets	808		PTT, PAI,	4T1	[122]
	MoO_{3-x} QDs	880	25.5%	PTT, PDT, PAI	HeLa	[85]
	L-Cys-$MoO_{2.8}$ NPs	808	41.24%	PTT		[74]
	D-Cys-$MoO_{2.8}$ NPs	808	34.67%	PTT		[74]
	L-Cys-$MoO_{2.3}$ NPs	808	37.31%	PTT		[74]
	D-Cys-$MoO_{2.3}$ NPs	808	32.27%	PTT		[74]
	L-Cys-MoO_2 NPs	808	43.25%	PTT		[74]
	D-Cys-MoO_2 NPs	808	36.26%	PTT		[74]
	L-Cys-MoO_{3-x} NPs	808	44%	PTT, PAI	HeLa	[23]
	WO_{3-x} @HA	1064	43.6%	PTT, PDT, PAI, CDT	4T1	[126]
	PEG-$W_{18}O_{49}$ NWs	808, 980		PTT, PDT	HeLa	[96]
	PEG-$WO_{2.9}$ NR	980		PTT, CT imaging	HeLa	[24]
	Chlorin-α-$SiMo_{12}O_{40}$	640–710		PDT		[114]
	BSA-$GdW_{10}O_{36}$	808		MR/CT imaging; PTT/radiotherapy		[70]
	Reduced [PMo_{12}]	808		PAI, PTT	4T1	[88]
	Oxidized [PMo_{12}]	808		PAI, PTT	4T1	[86]
	Mo_{154}	808		PTT, chemotherapy	4T1	[82]
	Mo_2C-derived POM	1060		PAI, PTT, CDT	HeLa	[89]
	Fe-POM	1060	58%	CDT, PTT	HeLa	[90]
	W-POM	808	58%	PTT	4T1	[87]
	CPI-POM	707		PDT		[115]
	[Mo_{154}] @VLPs	808		PTT		[91]
	Gd modified $Na_9GdW_{10}O_{36}$	808		MRI/CT, PTT		[99]
VIIB	BSA-MnO_2 NPs	810		PTT		[68]
	MCPF	808, 660		PTT, PDT	MCF-7	[69]
	MnO–CDs	635		PDT, FL, MRI	4T1	[130]
	MONs@PDA-ICG	808		PTT, PDT, MRI		[93]
VIIIB	Co_3O_4 NPs	808		PTT	U-87 MG	[94]
	PIONs	808		MRI, PTT, chemotherapy		[76]
	Fe_3O_4@PDA@BSA-Bi_2S_3	808	47.6%	MRI, PTT, CDT	HT29	[80]
	NOP-DOX@BSA-FA	655		PDT		[108]
IB	Au@SiO_2@ Cu_2O	670		PDT	MCF-7	[95]
IIB	UZNPs-PAA-DOX	808		PDT, chemotherapy, MRI	U14	[73]

[a] η represents of the value of photothermal conversion efficiency;
[b] SDT represents for sonodynamic therapy;
[c] PTT represents for Photothermal Therapy;
[d] PDT represents for photodynamic therapy;
[e] CDT represents for chemodynamic therapy;
[f] PAI represents for photoacoustic imaging;
[g] MRI represents for magnetic resonance imaging.

the conclusion that nanotherapeutic agents based on MONs@PDA have strong clinical application prospects in the treatment of liver cancers (Fig. 9D).

4. Summary and outlook

Similar to the development of medical science, the treatment of tumor is also iterative, and the emergence of phototherapy has become one of the latest and hottest topics. Transition metal oxide clusters with specific optical activity, such as PTT/PDT/PAI have become promising candidates in this fields. As mentioned above, numerous photosensitizers were reported to conduct the synergistic diagnosis and treatment in intravital tumors. The current developments of nanomaterials as phototherapy agents for tumor therapy are summarized as shown in Table 2.

Based on the works summarized above, we intend to conclude reasonable selection of inorganic oxide clusters and combination with different methods can contribute to enhance the efficient tumor treatment, as well as accelerate the clinical translation and development of inorganic nanomaterial-guided cancer therapy. Traditionally, the focuses of POM-based medicines are on the basis of cell wall/membrane disruption, inhibition of intracellular RCD activity, and depletion of GSH. However, more and more reports indicated the photo-enhanced synergistic effects.

Although transition metal nanocluster-based and POM-based nano-photosensitive agents/contrast agents possess respective merits at current stage, it is worth noting that the investigations of transition metal oxide nanoparticles in cancer research is still in its infancy, and still far from clinical transformation. The limitations, such as unknown long-term stability and biotoxicity, large doses of consumption, unaware of targeting effect, suboptimal tissue biodistribution and post-treatment cancer metastasis should be overcome. In addition, the related molecular mechanisms of inducing cell fate change during different treatment should also be interpreted. Therefore, progressive studies on systematic control over the synthesis as well as fundamental investigations on detailed mechanism of bio-optical activities along with new challenges concerning biosafety, long-term toxicity are still expected to be unveiled in the near future.

Declaration of competing interest

The authors declare that they have no known competing conflict of interests that could have appeared to influence this work reported in this review article.

Acknowledgments

This research was supported by grants from National Natural Science Foundation of China (No. 22101118), Shenyang Bureau of Science and technology (No. RC190167), Natural Science Foundation of Hubei Province (No. 2021CFB018).

References

[1] J. Chen, T. Fan, Z. Xie, et al., Biomaterials 237 (2020) 119827.
[2] Y.J. Hou, X.X. Yang, R.Q. Liu, et al., Int. J. Nanomed. 15 (2020) 6827–6838.
[3] Z. Yang, Z. Sun, Y. Ren, et al., Mol. Med. Rep. 20 (2019) 5–15.
[4] J. Yang, M. Hou, W. Sun, et al., Adv. Sci. 7 (2020) 2001088.
[5] S. Chen, B. Huang, W. Pei, et al., Int. J. Nanomed. 15 (2020) 8641–8658.
[6] H.L. Cheng, H.L. Guo, A.J. Xie, et al., J. Inorg. Biochem. 215 (2021) 111329.
[7] X. Ouyang, X. Wang, H.B. Kraatz, et al., Biomater. Sci. 8 (2020) 1160–1170.
[8] S. Rajkumar, M. Prabaharan, Curr. Top. Med. Chem. 17 (2017) 1858–1871.
[9] Y.C. Tsai, P. Vijayaraghavan, W.H. Chiang, et al., Theranostics 8 (2018) 1435–1448.
[10] Y. Wang, S. Luo, Y. Wu, et al., ACS Nano 14 (2020) 17046–17062.
[11] Z. Wei, P. Liang, J. Xie, et al., Chem. Sci. 10 (2019) 2778–2784.
[12] K. Wen, X. Xu, J. Chen, et al., ACS Appl. Mater. Interfaces 11 (2019) 17884–17893.
[13] M. Yang, S. Cao, X. Sun, et al., Bioconj. Chem. 31 (3) (2020) 663–672.
[14] J.M. Bae, H.M. Jung, B.Y. Hong, et al., JAMA Dermatol 153 (2017) 666–674.
[15] B. Ding, P. Zheng, F. Jiang, et al., Angew. Chem. Int. Ed. 59 (2020) 16381–16384.
[16] Y. Liu, P. Bhattarai, Z. Dai, et al., Chem. Soc. Rev. 48 (2019) 2053–2108.
[17] X. Wang, Z. Geng, H. Cong, et al., Chembiochem Eur. J. Chem. Biol. 20 (2019) 1628–1636.
[18] J. Xu, A. Gulzar, Y. Liu, et al., Small 13 (2017) 1701841.
[19] J. Nam, S. Son, L.J. Ochyl, et al., Nat. Commun. 9 (2018) 1074.
[20] L. Lilge, B.C. Wilson, J. Clinical Laser Med. Surg. 16 (1998) 81–91.
[21] D.K. Lakouas, D. Huglo, S. Mordon, M. Vermandel, Photodiag. Photodyn. Therapy 18 (2017) 236–243.
[22] N. Nyayapathi, J. Xia, J. Biomed. Optics 24 (2019) 1–13.
[23] J. Miao, Y. Cai, Y. Shao, et al., Appl. Mater. Today 23 (2021) 101001.
[24] Z. Zhou, B. Kong, C. Yu, et al., Sci. Rep. 4 (2014) 3653.
[25] M.H. Kim, H.Y. Son, G.Y. Kim, et al., Biomaterials 101 (2016) 121–130.
[26] R.S. Riley, E.S. Day, WIRES Nanomed. Nanobiotechnol. 9 (2017) e1449.
[27] W. Wei, X. Zhang, S. Zhang, G. Wei, Z. Su, Mater. Sci. Engin. C: Mater. Biol. Appl. 104 (2019) 109891.
[28] P. Chen, Y. Ma, Z. Zheng, et al., Nat. Commun. 10 (2019) 1192.
[29] F. Gong, L. Cheng, N. Yang, et al., Nano Lett. 18 (2018) 6037–6044.
[30] S. Liu, X. Pan, H. Liu, Angew. Chem. Int. Ed. 59 (2020) 5890–5900.
[31] M. Ji, M. Xu, W. Zhang, et al., Adv. Mater. 28 (2016) 3094–3101.
[32] J. Yang, H. Su, W. Sun, et al., Theranostics 8 (2018) 1966–1984.
[33] Z. Yang, R. Cheng, C. Zhao, Theranostics 8 (2018) 4097–4115.
[34] F. Gao, M. Sun, W. Ma, et al., Adv. Mater. 29 (2017) 1606864.
[35] P. Agostinis, K. Berg, K.A. Cengel, et al., Cancer J. Clinic. 61 (2011) 250–281.
[36] W. Fan, P. Huang, X. Chen, Chem. Soc. Rev. 45 (2016) 6488–6519.
[37] E. Cló, J.W. Snyder, P.R. Ogilby, K.V. Gothelf, Chembiochem. Eur, J. Chem. Biol. 8 (2007) 475–481.
[38] K. Watanabe, J. Tokumine, A.K. Lefor, et al., Sci. Rep. 11 (2021) 8432.
[39] W. Kong, L. Wang, Y. Zhao, et al., Nano Today 38 (2021) 101126.
[40] J. Lascaud, P. Dash, M. Würl, et al., Sci. Rep. 11 (2021) 2725.
[41] L. Golubewa, I. Timoshchenko, O. Romanov, Sci. Rep. 10 (2020) 22174.
[42] Y. Cheng, H. Zhang, Chemistry (Easton) 24 (2018) 17405–17418.
[43] Z. Zhang, Y. Cao, X. Zhu, Y. Li, X. Cai, ACS Biomater. Sci. Engin. 6 (2020) 4005–4011.
[44] A. Banerjee, G.E. Bertolesi, C.C. Ling, et al., ACS Appl. Mater. Interfaces 11 (2019) 13069–13078.
[45] S.L. Mekuria, K.D. Addisu, H.Y. Chou, B.Z. Hailemeskel, H.C. Tsai, Colloid. Surface. B: Biointerf. 167 (2018) 54–62.
[46] X. Yu, X. Yuan, Z. Huang, et al., ACS Biomater. Sci. Engin. 6 (2020) 6405–6414.
[47] Y. Liu, J. Li, M. Chen, X. Chen, N. Zheng, Theranostics 10 (2020) 10057–10074.
[48] K. Wang, Y. Zhang, J. Wang, et al., Sci. Rep. 6 (2016) 27421.
[49] W. Miao, G. Shim, S. Lee, Y.K. Oh, Biomaterials 35 (2014) 4058–4065.
[50] Y. Xu, Y. Shan, H. Cong, Y. Shen, B. Yu, Curr. Pharm. Design 24 (2018) 4060–4076.
[51] H.J. Ryu, W.K. Lee, Y.H. Kim, J.S. Lee, Mikrochim. Acta 188 (2021) 164.
[52] W. Jin, L. Hu, Nanomaterials 9 (2019) 1359.
[53] Y. Zhang, F. Zhang, H. Wang, et al., Opt Express 27 (2019) 7935–7944.
[54] C. Liu, Y. Cao, Y. Cheng, et al., Nat. Commun. 11 (2020) 1735.
[55] Y.M. Sun, W. Akram, F. Cheng, et al., Bioorg. Chem. 90 (2019) 103085.
[56] J. Wen, K. Yang, S. Sun, Chem. Commun. 56 (2020) 7065–7079.
[57] L. Zhang, Q. Cheng, C. Li, X. Zeng, X.Z. Zhang, Biomaterials 248 (2020) 120029.
[58] J. Liu, H. Liang, M. Li, et al., Biomaterials 157 (2018) 107–124.
[59] Y. Shao, B. Liu, Z. Di, et al., J. Am. Chem. Soc. 142 (2020) 3939–3946.
[60] B. Liao, S. Li, G. Yang, Inorg. Chem. 60 (2021) 1839–1845.
[61] Q. Wang, H. Tian, Z. Zhang, et al., Chin. Chem. Lett. (2021), doi:10.1016/j.cclet.2021.09.079.
[62] N. Li, J. Liu, J.J. Liu, et al., Angew. Chem. Int. Ed. 58 (2019) 17260–17264.
[63] T. Liu, E. Diemann, H. Li, A.W.M. Dress, A. Müller, Nature 426 (2003) 59–62.
[64] M. Zhao, X.Y. Zhu, Y.Z. Li, et al., Tungsten 4 (2022) 121–129.
[65] H. Zhang, R. Shi, A. Xie, et al., ACS Appl. Mater. Interfaces 5 (2013) 12317–12322.
[66] Y. Tian, W. Yi, L. Bai, et al., Int. J. Biolog. Macromol. 137 (2019) 904–911.
[67] W. Zhu, Z. Dong, T. Fu, et al., Adv. Funct. Mater. 26 (2016) 5490–5498.
[68] Y. Wang, Y. Song, G. Zhu, D. Zhang, X. Liu, Chin. Chem. Lett. 29 (2018) 1685–1688.
[69] W. Zeng, H. Zhang, Y. Deng, et al., Chem. Engin. J. 389 (2020) 124494.
[70] Y. Yong, L. Zhou, S. Zhang, et al., NPG Asia Mater 8 (2016) e273.
[71] M. Ramezani-Aliakbari, J. Varshosaz, H. Sadeghi-aliabadi, F. Hassanzadeh, M. Rostami, Langmuir 37 (2021) 6475–6489.
[72] S. Feng, Y. Mao, X. Wang, et al., J. Colloid Interface Sci. 559 (2020) 51–64.
[73] Q. Cai, D. Yang, L. Zhong, P. Yang, Chem. Mater. 32 (2020) 7492–7506.
[74] Y. Li, Z. Miao, Z. Shang, et al., Adv. Funct. Mater. 30 (2020) 1906311.
[75] Z. Guo, J. Xu, J. Zhang, et al., ACS Appl. Bio. Mater. 1 (2018) 367–373.
[76] Y. Hu, H. Hu, J. Yan, et al., Bioconj. Chem. 29 (2018) 1283–1290.
[77] G. Wang, W. Gao, X. Zhang, X. Mei, Sci. Rep. 6 (2016) 28258.
[78] J. Li, Y. Hu, J. Yang, Biomaterials 38 (2015) 10–21.
[79] S. Shen, S. Wang, R. Zheng, et al., Biomaterials 39 (2015) 67–74.
[80] K. Luo, J. Zhao, C. Jia, ACS Appl. Mater. Interfaces 12 (2020) 22650–22660.
[81] M. Yuan, S. Xu, Q. Zhang, et al., Chem. Engin. J. 394 (2020) 124874.
[82] S. Zhang, H. Chen, G. Zhang, et al., J. Mater. Chem. B 6 (2018) 241–248.
[83] S. Zhang, B. Peng, P. Xue, et al., Soft Matter 15 (2019) 5375–5379.
[84] D. Ni, D. Jiang, H.F. Valdovinos, et al., Nano Lett. 17 (2017) 3282–3289.
[85] D. Ding, W. Guo, C. Guo, et al., Nanoscale 9 (2017) 2020–2029.
[86] Y. Yong, C. Zhang, Z. Gu, et al., ACS Nano 11 (2017) 7164–7176.
[87] J. Zhou, W. Zhao, Z. Miao, et al., ACS Nano 14 (2020) 2126–2136.
[88] C. Zhang, W. Bu, D. Ni, et al., J. Am. Chem. Soc. 138 (2016) 8156–8164.
[89] G. Liu, J. Zhu, H. Guo, et al., Angew. Chem. Int. Ed. 58 (2019) 18641–18646.
[90] Y. Shi, J. Zhang, H. Huang, et al., Adv. Healthcare Mater. 9 (2020) 2000005.
[91] Y.R. Xue, Y. Wang, G. Chen, et al., Biomater. Sci. 9 (2021) 3875–3883.
[92] Z. Liu, S. Zhang, H. Lin, et al., Biomaterials 155 (2018) 54–63.
[93] Y. Zhu, M. Deng, N. Xu, Y. Xie, X. Zhang, Front. Chem. 9 (2021) 650899.
[94] X. Huang, H. Cai, H. Zhou, et al., Acta Biomater. 121 (2021) 605–620.
[95] C. Liu, H. Dong, N. Wu, et al., ACS Appl. Mater. Interfaces 10 (2018) 6991–7002.
[96] P. Kalluru, R. Vankayala, C.S. Chiang, K.C. Hwang, Angew. Chem. Int. Ed. 52 (2013) 12332–123326.
[97] J. Liu, Q. Chen, W. Zhu, et al., Adv. Funct. Mater. 27 (2017) 1605926.
[98] J. Li, Z. Chen, M. Zhou, et al., Angew. Chem. Int. Ed. 55 (2016) 2592–2595.
[99] S. Zhang, M. Li, Y. Zhang, et al., Dalton Trans. 50 (2021) 8076–8083.
[100] S. Zhang, Y. Zheng, S. Yin, et al., Chem. Eur. J. 23 (2017) 2802–2810.
[101] L. Vandebroek, E. DeZitter, H.G.T. Ly, et al., Chem. Eur. J. 24 (2018) 10099–10108.
[102] G.P. Yang, X. Wu, B. Yu, C.W. Hu, et al., ACS Sustain. Chem. Engin. 7 (2019) 3727–3732.
[103] S. She, S. Bian, R. Huo, et al., Sci. Rep. 6 (2016) 33529.
[104] Y. Gu, Q. Li, Y. Huang, et al., Chem. Commun. 56 (2020) 2869–2872.
[105] W.R. Stefan, K. Hong Pyo, H. Alexander, et al., Antioxidants Redox Signal 9 (2007) 49–89.
[106] S. Fu, Y. Man, F. Jia, et al., J. Nanomater. 2020 (2020) 2832347.
[107] C.C. Barrera, H. Groot, W.L. Vargas, D.M. Narváez, Int. J. Nanomed. 15 (2020) 6421–6432.
[108] S. Bano, S. Nazir, S. Munir, et al., Int. J. Nanomed. 11 (2016) 3159–3166.
[109] Y. Zu, H. Yao, Y. Wang, et al., View 2 (2021) 20200188.
[110] M. Lv, Y. Liu, K. Li, G. Yang, Tetrahedron Lett. 65 (2021) 152757.
[111] G. Yang, K. Li, X. Lin, et al., Chin. J. Chem. 39 (2021) 3017–3022.
[112] G.P. Yang, X.L. Zhang, Y.F. Liu, et al., Inorg. Chem. Front. 8 (2021) 4650–4656.
[113] M. Zhao, X. Chen, G. Chi, et al., Inorg. Chem. Front. 7 (2020) 4320–4332.
[114] I. Yoon, J.H. Kim, J.Z. Li, W.K. Lee, Y.K. Shim, Inorg. Chem. 53 (2014) 3–5.
[115] T.H. Lee, Y. Liu, H.J. Kim, et al., Eur. J. Inorg. Chem. 2021 (2021) 3211–3223.
[116] P. Yin, L. Jin, D. Li, et al., Chem. Eur. J. 18 (2012) 6754–6758.
[117] J. Zhang, Y. Liu, Y. Li, H. Zhao, X. Wan, Angew. Chem. Int. Ed. 51 (2012) 4598–4602.
[118] D. Jia, L. Gong, Y. Li, et al., Angew. Chem. Int. Ed. 60 (2021) 21449–21456.
[119] L. Gong, W. Ding, Y. Chen, et al., Angew. Chem. Int. Ed. 60 (2021) 8344–8351.
[120] L. Wang, S. Li, Y. Kai, Adv. Healthcare Mater. 8 (2019) 1900471.
[121] Q. Liu, C. Sun, Q. He, et al., Chem. Commun. 51 (2015) 10054–10057.
[122] G. Song, J. Hao, C. Liang, et al., Angew. Chem. Int. Ed. 55 (2016) 2122–2126.
[123] J. Wang, X. Wu, W. Ma, C. Xu, Adv. Funct. Mater. 30 (2020) 2000670.
[124] Y. Xing, Y. Cai, J. Cheng, X. Xu, Appl. Nanosci. 10 (2020) 2069–2083.
[125] C. Gautier, T. Bürgi, J. Am. Chem. Soc. 128 (2006) 11079–11087.
[126] Y. Ding, R. Huang, L. Luo, et al., Inorg. Chem. Front. 8 (2021) 636–646.
[127] G. Ou, Z. Li, D. Li, et al., Nano Res. 9 (2016) 1236–1243.
[128] D. Yang, G. Yang, Q. Sun, Adv. Healthc Mater. 7 (2018) e1800042.
[129] B. Ding, P. Zheng, P.A. Ma, J. Lin, Adv. Mater. 32 (2020) 1905823.
[130] Q. Jia, J. Ge, W. Liu, et al., Adv. Mater. 30 (2018) 1706090.